On boundary-layer separation and internal wave generation at the Knight Inlet sill

By Kevin G. Lamb

University of Waterloo, Waterloo, Ontario N2L 3G1,
Canada (kglamb@math.uwaterloo.ca)

This paper reports results of numerical simulations of stratified tidal flow over the Knight Inlet sill. A non-hydrostatic, two-dimensional model is used, which incorporates a no-slip bottom boundary condition through the use of a vertical eddy viscosity/diffusivity parametrization that is non-zero only near the bottom. In inviscid model runs, a large lee wave is rapidly formed, which quickly breaks, leading to the formation of a high-drag state and a strong downslope jet in the early stages of the ebb tide. The use of a no-slip bottom boundary condition results in boundary-layer separation from near the top of the sill. This significantly reduces the amplitude of the lee wave during the initial stages of the flow development. For most model runs, a large lee wave is ultimately formed and the separation point moves down the lee of the sill to a position immediately downstream of the lee wave. The transition to this high-drag state is significantly delayed compared with inviscid model runs. Weakened stratification immediately above the sill, inclusion of an eddy viscosity/diffusivity above the bottom and a pool of dense water on the downstream (seaward) side of the sill can all contribute to a delay in the transition to a high-drag state, and can eliminate it entirely. For one model run using a vertical eddy viscosity parametrization above the bottom, a reduction of the vertical diffusivity eliminated the formation of a high-drag state. This suggests that at least in some cases entrainment into the lee wave can cause its growth and result in the formation of a high-drag state.

1. Introduction

Stratified flow over topography has been a prominent problem in geophysical fluid mechanics for over 50 years since Queney (1948) first investigated internal wave generation in stratified flow over a mountain. A particular problem that has received a considerable amount of attention is that of stratified flow over a large obstacle and the formation of a high-drag state. A high-drag state consists of a strong, supercritical downslope jet of fluid beneath a large breaking lee wave. The strong downslope flow results in a low-pressure region along the lee of the obstacle and hence in a net horizontal force (drag) on the obstacle. This flow phenomenon has a hydraulic

interpretation. A control point near the top of the obstacle separates upstream subcritical flow from the supercritical downslope jet. The jet ends in a hydraulic jump downstream of the obstacle. In the atmospheric context the jet is referred to as a downslope windstorm. There are many atmospheric observations of strong downslope windstorms (Baines 1995). Oceanic observations are much more recent and sparse (Farmer & Armi 1999; Nash & Moum 2001).

Atmospheric observations of a downslope wind storm on 11 January 1972 in Boulder, CO, USA (Klemp & Lilly 1975) led to a series of papers reporting the results of numerical simulations which explored various aspects of this event (e.g. Klemp & Lilly 1975; Peltier & Clark 1979; Hoinka 1985; Scinocca & Peltier 1989). These numerical simulations of the high-drag state agreed well in detail with the observations. As the atmospheric observations of this event were limited to the final high-drag state, our understanding of the formation of high-drag states has, until recently, been based solely on the results of these, and other, numerical simulations.

In 1995 the Knight Inlet experiment provided field observations of tidal flow over a large sill in Knight Inlet (Farmer & Armi 1999; Klymak & Gregg 2001, 2003; Armi & Farmer 2002). This sill has been the site of previous field experiments (Farmer & Smith 1980; Farmer & Freeland 1983). It provides a natural laboratory for studying stratified flow over a large obstacle. At the location of the sill the inlet is approximately straight, and modelling studies have usually treated ebb flow as being two dimensional. The flood tide is more three dimensional, due to a widening of the sill on the seaward side. The three-dimensional (3D) nature of the flow over the sill has been investigated by Klymak & Gregg (2001).

The highly resolved set of field observations reported by Farmer & Armi (1999) (henceforth FA99) include observations of the formation of a high-drag state during ebb flow over the sill. Their observations led them to suggest a new mechanism for the formation of the high-drag state. This has led to a series of papers reporting results of numerical simulations aimed at understanding the nature of the flow over the Knight Inlet sill (Cummins 2000; Afanasyev & Peltier 2001a). The interpretation of the numerical results and the observations has been somewhat controversial (Farmer & Armi 2001; Afanasyev & Peltier 2001b).

FA99 reported observations of small-scale waves and mixing near the surface above the sill during the early stages of ebb tide. In addition, flow separation from the top of the sill was observed. Flow separation, which persisted for over half of ebb tide, was also a common feature of earlier observations taken over the sill (Farmer & Smith 1980; Farmer & Freeland 1983). There was apparently no evidence of the generation of a lee wave early in the tidal flow. FA99 argued that the small-scale waves above the sill were the result of shear instabilities, a consequence of a shear flow induced by the mode-1 response to the subcritical flow over the sill. They further argue that the associated mixing led to the formation of a wedge of slow-moving fluid above the lee of the sill. Shear instabilities on the interface between this intermediate layer and the rapidly moving fluid below persist throughout ebb tide. Using observations of the density and velocity fields, FA99 estimate that the volume of fluid entrained across the interface can account completely for the increase in volume of the intermediate layer. The high pressure associated with the growing wedge of slowly moving fluid pushes the separation point down the lee of the sill, resulting in the formation of a high-drag state late in ebb tide. This mechanism for the formation of a high-drag state is novel and very different from that seen in the inviscid numerical simulations of

the downslope windstorm in Boulder, CO. These simulations showed the generation of a large internal lee wave which rapidly grows in amplitude until it overturns. As a consequence, a large region of nearly stagnant, mixed fluid is created, below which a downslope jet is formed.

Cummins (2000) used the Princeton Ocean Model (POM), run as a two-dimensional model, to simulate tidal flow over the Knight Inlet sill. The POM is hydrostatic and incorporates a sophisticated turbulence model. A quadratic drag law is used as a bottom boundary condition for the velocity field. Cummins used realistic topography and a density field based on observations 1.2 km inland of the sill. Afanasyev & Peltier (2001a), on the other hand, used a non-hydrostatic inviscid model with idealized topography.

Both these modelling studies showed the early formation of a large lee wave which formed a patch of slowly moving fluid above the lee slope. Below the wave, a strong downslope jet was formed. The simulations reported by Cummins did not have a breaking lee wave, due to the strong mixing invoked by the turbulence model. The flow did not separate, and the downslope jet was formed much earlier than in the observations. Cummins attributed the earlier formation of the high-drag state to the absence of flow separation. To test this idea he did a simulation using modified topography in which the lower boundary was raised downstream of the sill in order to mimic some of the expected effects of boundary-layer separation. This had the effect of significantly reducing the amplitude of the lee wave and delayed the formation of the high-drag state. The simulations of Afanasyev & Peltier also did not have boundary-layer separation, this being impossible in an inviscid model. The lee wave formed in their simulations overturned rapidly and quickly led to the formation of a high-drag state. In essence, their results duplicated those of the simulations of the Boulder, CO, windstorm reported earlier.

Gheusi *et al*. (2000) have done some low-Reynolds-number ($Re = 200$), two- and three-dimensional direct numerical simulation calculations of stratified flow over an obstacle. They used a non-hydrostatic model with a no-slip bottom boundary condition and considered flow of a uniformly stratified fluid of depth large compared with the obstacle amplitude. They found that boundary-layer separation significantly modified the evolution of the flow. Their 3D simulations also showed that 3D effects are important after the wave breaks. The three-dimensionalization of the flow in breaking internal gravity waves is well known (e.g. Klaasen & Peltier 1985; Caulfield & Peltier 1994; Winters & D'Asaro 1994). Two mechanisms have been identified: shear instabilities and convective instabilities (Winters & D'Asaro 1994).

Klymak & Gregg (2003) have suggested that a density difference across the sill is responsible for the flow separation. The water on the seaward side of the sill is denser, with the largest density differences, $ca.\,0.5\,\mathrm{kg\,m^{-3}}$, occurring below the sill crest. They argue that during ebb flow, water flowing over the sill encounters the slightly denser water below the sill crest and is forced to separate.

In this paper the results of some numerical simulations of tidal flow over the Knight Inlet sill are reported. A two-dimensional, non-hydrostatic model (Lamb 1994) is used. An important difference between these simulations and those of Cummins (2000) and of Afanasyev & Peltier (2001a) is the use of vertical eddy viscosity and diffusion, which allows the incorporation of a no-slip bottom boundary condition. The resulting formation of a bottom boundary layer enables flow separation to occur, which is a significant step towards the goal of accurate numerical simulations of the

flow over the sill in Knight Inlet. In the model simulations with vertical viscosity, the flow separates during the early part of the ebb tide. A lee wave is formed which breaks and a pool of near-surface slow-moving fluid is formed. In most cases this nearly stagnant patch of fluid grows and as a consequence the separation point moves down the lee slope of the sill. The final high-drag state which is formed consists of a strong downslope jet beneath a large lee wave. Post-wave separation (Baines 1995) occurs, in which the downslope flow leaves the sill just downstream of the large lee wave. The results reported herein largely confirm the mechanism for the generation of a high-drag state first put forth by Peltier & Clark (1979). That is, it appears to be tied to the generation of a large amplitude lee wave directly created by flow over the sill. However, it is also demonstrated that the results are sensitive to some of the details of the stratification, the background currents and the form of the vertical viscosity. Such a sensitivity has been observed. For example, Farmer & Smith (1980) report a wide variety of responses to flow over the sill. Results of a model run using a reduced stratification immediately above the sill and a Richardson-based eddy viscosity/diffusivity parametrization show that under some circumstances a high-drag state is never reached. It is furthermore shown that, by increasing the vertical eddy diffusivity, a large lee wave is generated, and transition to a high-drag state does occur. This shows that mixing can play an important role in the formation of a high-drag state, as argued by FA99.

In § 2 the numerical model is described. In § 3, unstratified flow over the sill is discussed. Both inviscid and viscous flows are considered. The inviscid, unstratified flow over the sill is potential flow. This provides the outer flow used in boundary-layer theory to predict the time and location of flow separation. Predictions of a simple theory due to Blasius (1908) are compared with numerical model results. These unstratified model simulations aid the interpretation of the stratified simulations.

Four model runs, discussed in § 4, compare the flow evolution with and without vertical diffusion/viscosity and with and without a deep water density pool. These simulations show that the use of a vertical viscosity and a no-slip bottom boundary condition is essential to trigger separation of the bottom boundary layer. The observed density difference across the sill enhances flow separation, but cannot by itself force the flow to separate. Thus, the cross-sill density jump is of secondary importance. In § 5 the sensitivity of the results to the stratification and to the vertical viscosity/diffusion parametrization is explored. The majority of the model runs were started from a state of rest at the beginning of ebb tide. Results of a couple of longer model runs are also discussed. Finally, the results are summarized and discussed in § 6. The simulations reported here fail to model some aspects of the observed features, in particular the small-scale instabilities and the entrainment process which FA99 argue leads to the formation of a high-drag state. A discussion of this is included in § 6.

2. The numerical model

The numerical model used in this study is a modified version of the non-hydrostatic model described in Lamb (1994), which uses the Boussinesq approximation. A rigid lid is used at the surface at $z = 0$. A crude turbulence model has been added in the form of vertical eddy diffusion and viscosity. Its main purpose is to form a bottom boundary layer (BBL) by slowing fluid near the bottom boundary, this being the most

crucial contributor to flow separation. Rotation is not included for these simulations, as Knight Inlet is only a few kilometres across. The model equations are

$$\boldsymbol{U}_t + \boldsymbol{U} \cdot \nabla \boldsymbol{U} = -\nabla p - \rho g \hat{k} + (K_u \boldsymbol{U}_z)_z + M \boldsymbol{U}_{\chi\chi}, \tag{2.1}$$

$$\rho_t + \boldsymbol{U} \cdot \nabla \rho = (K_\rho \rho_z)_z + M \rho_{\chi\chi}, \tag{2.2}$$

$$\nabla \cdot \boldsymbol{U} = 0, \tag{2.3}$$

where standard terminology has been used and p and ρ have been scaled by the reference density ρ_0. Terrain following (sigma) coordinates are used and χ is the horizontal terrain-following coordinate. The horizontal diffusivity/viscosity M acts along sigma levels as in the POM (Mellor & Yamada 1985). Some model runs with values of M no larger than 5×10^{-3} were done. As these results differed only slightly from corresponding runs with $M = 0$, all results reported here use $M = 0$. The formulation of the model allows K_u and K_ρ to vary spatially and temporally. In this paper they are usually specified functions of z only. For some model runs these specified values are augmented by a Richardson-number-based parametrization of the form used by Pacanowski & Philander (1981). The latter gives temporally and spatially varying values and is used only to explore the sensitivity of the results. Parametrizations of this form were developed for use in low-resolution hydrostatic models and hence may seem unnecessary in a non-hydrostatic model. The model used here, however, will fail to accurately simulate small-scale instabilities because of both inadequate resolution and the fact that the model is two-dimensional. Boundary conditions in the vertical are $\rho_z = 0$ along the top and bottom boundaries, and $u_z = 0$ along the top boundary with a no-slip condition along the bottom boundary. Use of a no-slip condition, rather than a quadratic stress law, was found to be essential for flow separation. For the inviscid version of the model, $K_u = K_\rho = M = 0$ and the boundary conditions along the upper and lower boundaries are those of no normal flow. Horizontal resolutions between 10 and 1 m over the sill have been used. There are J grid points in the vertical with J typically 100. Most of the model runs used a vertically uniform grid. Some model runs were done using a vertically varying grid, with higher resolution at the bottom. There was very little difference between such runs and the corresponding run using a vertically uniform grid.

The model topography used is

$$
\begin{aligned}
z = h(x_k) \\
= -200 + 67\,\mathrm{itanh}(x_k, 10.45, 0.05) \\
- 50\,\mathrm{itanh}(x_k, 10.94, 0.08) + 112\,\mathrm{itanh}(x_k, 11.91, 0.08) \\
- 119\,\mathrm{itanh}(x_k, 12.015, 0.06) - 160\,\mathrm{itanh}(x_k, 12.8, 0.04) \\
+ 125\,\mathrm{itanh}(x_k, 13.01, 0.08) + 25\,\mathrm{itanh}(x_k, 13.6, 0.08), \quad (2.4)
\end{aligned}
$$

where $x_k = x/1000$ is in km and

$$\mathrm{itanh}(x_k, a, s) = \int_{-\infty}^{x_k} 1 + \tanh\left(\frac{x_k' - a}{s}\right) \mathrm{d}x_k' = x_k - a + s \ln\left(2\cosh\frac{x_k - a}{s}\right). \tag{2.5}$$

The model topography is compared with the observed topography in figure 1. The topography has been levelled at depths of 200 and 150 m on the landward/seaward sides of the sill. The sill is asymmetric with a maximum slope of 0.3 near the top of
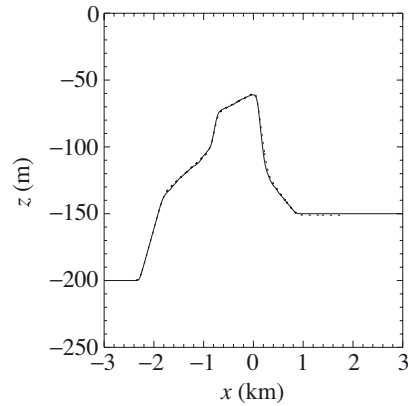
Figure 1. Comparison of model topography (solid curve)
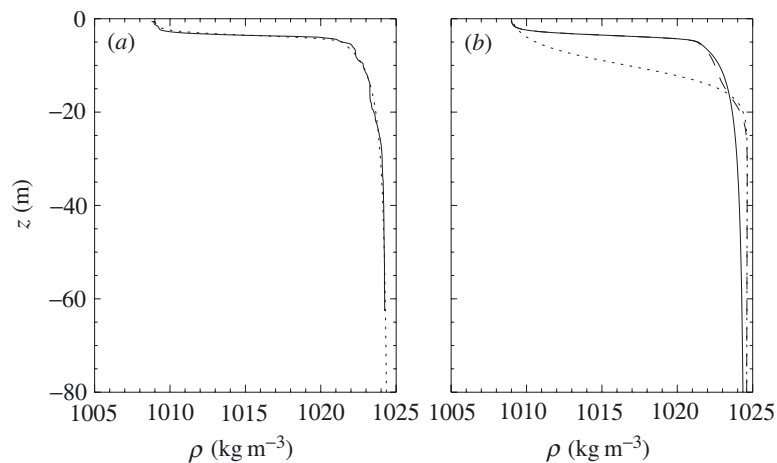and observed topography (dotted curve).

Figure 2. Model densities. (*a*) Comparison of model density $\bar{\rho}_1(z)$ (dotted curve) with the observed density 1.2 km from the sill (solid curve). (*b*) Comparison of three model densities: $\bar{\rho}_1(z)$ (solid line), $\bar{\rho}_2(z; -10, 5)$ (dotted line), $\bar{\rho}_3(z)$ (dashed line).

the sill on the seaward side. The steep slope is conducive to boundary-layer separation during ebb tide.

Several density stratifications have been used. The first stratification used is a fit to a mean density field observed 1.2 km upstream of the sill during ebb tide and so may have been influenced by upstream effects. It is given by

$$\rho_0 \bar{\rho}_1(z) = \frac{1}{2}\Bigg[(1024.0 - 7.5(1 + \tanh(z + 4)))(1.0 + \tanh(z + 4.0))$$
$$+ \left(1024.6 + \frac{20.0}{z - 1}\right)(1.0 - \tanh(z + 4.0))\Bigg]. \quad (2.6)$$

The reference density used in making the Boussinesq approximation is $\rho_0 = 1016.5 \text{ kg m}^{-3}$. Density $\bar{\rho}_1$ is compared with the observed density in figure 2*a*. Note the thin surface cap of fresh water formed by river run-off.
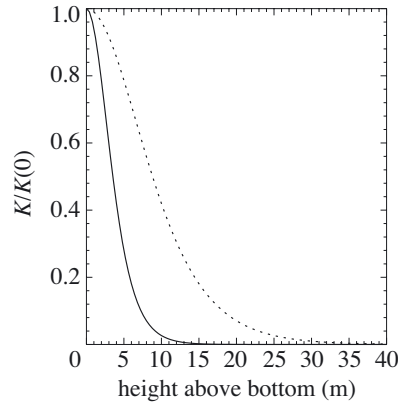
Figure 3. Vertical profiles of the vertical eddy viscosity/diffusivity given by equation (2.10) for $\alpha = 0.25$ m^{-1} (solid line) and 0.1 m^{-1} (dotted line).

A number of alternative density fields were considered, all modifications of (2.6). First, a class of density fields was defined via

$$\bar{\rho}_2(z; z_0, d) = a + bz + s\left[1 + \tanh\left(\frac{z - z_0}{d}\right)\right]. \tag{2.7}$$

The values $a = 1.008$ and $b = 8.125 \times 10^{-7}$ m^{-1} were chosen to match the density and density gradient values at $z = -200$ m with those of $\bar{\rho}_1$ given by (2.6). For specified values of z_0 and d, the value of s was chosen so that $\bar{\rho}_2(0) = \bar{\rho}_1(0)$. In figure 2b $\rho_0\bar{\rho}_1(z)$ and $\rho_0\bar{\rho}_2(z)$ are compared using $(z_0, d) = (-10, 5)$ m. Density $\bar{\rho}_2(z)$ has a weaker gradient at depths greater than 20 m and has a broader, weaker pycnocline. It is also missing the upper mixed layer.

The model results using densities (2.6) and (2.7) with $(z_0, d) = (-10, 5)$ m were quite different. The difference is due to the decreased stratification immediately above the sill, i.e. at depths greater than 20 m. To illustrate this a third density field was used, which is a weighted average of $\bar{\rho}_1(z)$ and $\bar{\rho}_2(z)$, namely

$$\bar{\rho}_3(z) = r\bar{\rho}_1(z) + (1 - r)\bar{\rho}_2(z; -10, 5), \tag{2.8}$$

where

$$r(z) = 0.5\left(1 + \tanh\left(\frac{z + 17.5}{5.0}\right)\right), \tag{2.9}$$

density $\bar{\rho}_3(z)$ is equal to $\bar{\rho}_2(z; -10, 5)$ for z below $ca. -22.5$ m and is equal to $\bar{\rho}_1$ for z greater than $ca. -12.5$ m. It is also plotted in figure 2.

The temporally fixed, vertically varying eddy viscosity and diffusivity K_u and K_ρ have the form

$$K_{u,\rho}(x, z) = C_{u,\rho} \operatorname{sech}^2(\alpha(z - h(x_k))), \tag{2.10}$$

where C_u is a constant. Values of α between 0 and 0.5 m^{-1} have been used. When $\alpha = 0$, the vertical viscosity/diffusivity is constant. For $\alpha = 0.25$ m^{-1}, $K_{u,\rho}$ are reduced to 20% of their maximum value $ca. 5$ m above the bottom (see figure 3). This is the base value. It gives a boundary-layer thickness of $ca. 5$ m at peak tidal flow. Some model runs were done using profiles of $K_{u,\rho}$ which are constant, or increase

Table 1. *Model runs discussed in the text*

(Under BBL, yes (no) means that there is (is not) a bottom boundary layer. PP refers to use of Richardson-number-based eddy viscosity/diffusivity above the bottom. $\Delta\bar{\rho}$ refers to the use of a density jump across the sill. The jump extends above the sill crest in cases I and K but is restricted to below the crest in cases E and F.)

case	$\bar{\rho}$	BBL	PP	$\Delta\bar{\rho}$	t_{end}
A	const.	no	no	no	0.5τ
B	const.	yes	no	no	0.5τ
C	$\bar{\rho}_1$	no	no	no	0.5τ
D	$\bar{\rho}_1$	yes	no	no	0.5τ
E	$\bar{\rho}_1$	yes	no	yes	0.5τ
F	$\bar{\rho}_1$	yes	no	yes	0.5τ
G	$\bar{\rho}_3$	yes	no	no	0.5τ
H	$\bar{\rho}_3$	yes	yes	no	0.5τ
I	$\bar{\rho}_3$	yes	yes	yes	0.5τ
J	$\bar{\rho}_1$	yes	no	no	1.5τ
K	$\bar{\rho}_3$	yes	yes	yes	1.0τ

linearly, in the first 10 m above the bottom before rapidly dropping off to zero. The results were very similar to those using (2.10).

All model runs are started from a state of rest. The flow is driven by specifying values of u_t at the left boundary. Sinusoidal tidal flow with a period of $\tau = 12.4\,\mathrm{h}$ is used throughout. Unless otherwise specified, model runs commence at the start of ebb tide. They all use a peak volume flux of $36\,\mathrm{m}^2\,\mathrm{s}^{-1}$, based on observations. This gives a peak barotropic tidal flow of $0.6\,\mathrm{m}\,\mathrm{s}^{-1}$ at the sill crest. Tidal advection distances are $4.3\,\mathrm{km}$ at the sill crest and $1.3\,\mathrm{km}$ in the deep water. These distances are comparable to the sill width. For density $\bar{\rho}_1(z)$, Froude numbers U/c at the sill crest at maximum ebb are 0.9 and 2.0 for mode-1 and mode-2 waves. Here U and c are the barotropic current and linear long-wave propagation speed, respectively. Since the calculation of these numbers uses the initial undisturbed density field and assumes no vertical structure in the horizontal currents, assumptions not valid at peak ebb tide, they should be used as a guide only: the peak ebb flow is subcritical for mode-1 waves and supercritical to mode-2 waves.

3. Unstratified flow over the sill

Internal waves are a consequence of the gravitational adjustment of vertical displacements of a stratified fluid. In inviscid flow over a sill, the flow field that creates the initial disturbances is a potential flow. Thus, before considering the problem of stratified flow over the sill it is instructive to consider some aspects of the unstratified problem: specifically, potential flow over the sill for the inviscid case and boundary-layer separation in the absence of stratification for the case with vertical viscosity.

Figure 4 illustrates the potential flow over the sill, determined by running the inviscid version of the model with gravity set to zero (case A, see table 1). Density contours, used as a tracer to visualize fluid advection, are shown in figure 4*a, b*. Contour plots of the horizontal and vertical velocities are presented in figure 4*c, d*. Only part of the computational domain is shown in the figures. That the results accurately
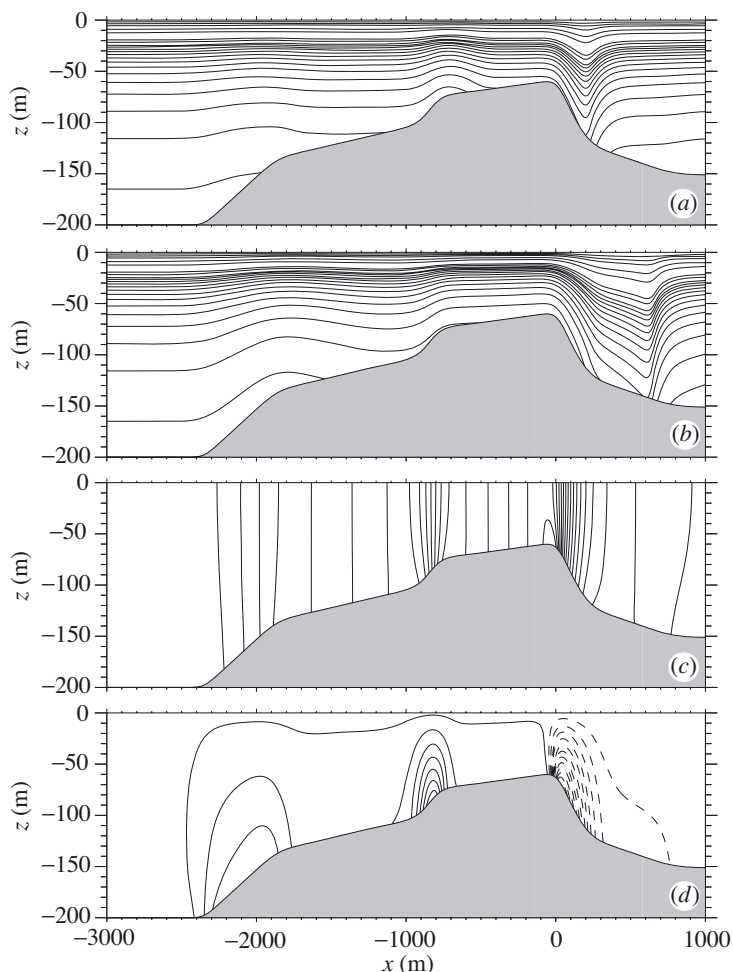
Figure 4. Potential flow over the sill (case A). (*a*), (*b*) Density contours (used as a tracer) at $t = \tau/16$ and $\tau/8$. (*c*), (*d*) Horizontal and vertical velocity contours (solid contours positive values, dashed contours negative values) at $t = \tau/8$.

approximate potential flow in a horizontally unbounded domain was verified by running the model for several resolutions and for different locations of the left and right boundaries.

The first density contour plot shows the displacements at $t = \tau/16 = 2790$ s. At this time, horizontal displacement of fluid is 32 m at the top of the sill and less in greater depths. This distance is small compared with the horizontal scale of the sill and, in particular, with the width of the downwelling zone in the lee of the sill. Hence, the vertical displacement pattern largely reflects the pattern of the vertical velocity shown in figure 4*d*. At $t = \tau/8$ (figure 4*b*), the horizontal advection distance has increased to 1.2 km at the top of the sill, and 0.5 km in water of depth 150 m. The displacement pattern no longer reflects the vertical velocity field.

For the stratified cases considered in the next section, the mode-1 propagation speed is smallest on top of the sill where it is *ca.* $0.66 \, \mathrm{m \, s^{-1}}$. The time taken to
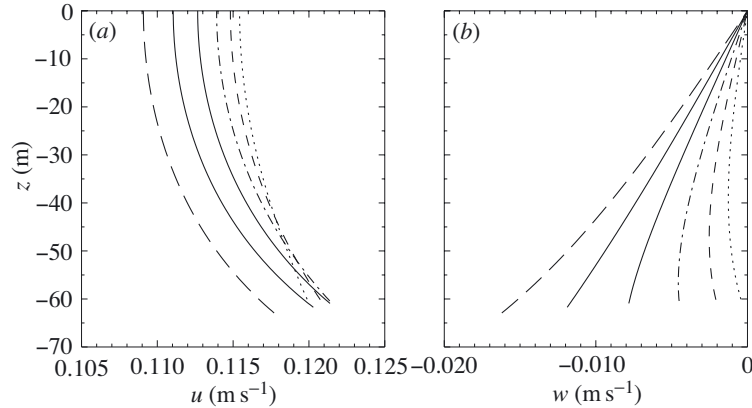
Figure 5. Potential flow over the sill. Vertical profiles of (*a*) the horizontal velocity, (*b*) the vertical velocity at $t = 1395$ s. Profiles in (*b*) are, from left to right, at 10 m intervals between $x = 0$ and $x = -50$ m. Profiles in (*a*) are at the same locations using the same line styles.

propagate 200 m is 300 s on top of the sill and less in deeper water. Thus, in the presence of gravity, it is clear that wave propagation will substantially modify the vertical displacement and velocity fields in the lee of the sill by $t = \tau/16$.

Figure 5 shows vertical profiles of the horizontal and vertical velocity at 10 m intervals between $x = -50$ m and $x = 0$. The crest of the sill is at $x = -54$ m. The potential flow horizontal velocity has vertical shear with maximum horizontal velocities occurring at the bottom at about $x = -25$ m. Surface values are *ca.* 7% smaller than those at the bottom at this location. The vertical velocities have their maximum absolute values at the bottom, decreasing approximately linearly to zero at the surface. The largest downwelling velocity of -0.025 m s^{-1} occurs at $x = 44$ m, 32 m below the sill crest (not shown).

Profiles of some features of the flow along the bottom boundary in the vicinity of the sill crest are presented in figure 6. For reference, the topography in the vicinity of the sill crest is shown in figure 6*a*. Figure 6*b* shows the horizontal velocity u and the tangential component of the velocity $q = \hat{t} \cdot \boldsymbol{U}$ at $t = \tau/16$. Here $\hat{t}$ is the rightward pointing unit tangent vector along the bottom boundary. Since q is positive during ebb tide, it is the fluid speed along the bottom boundary. Its maximum occurs at about $x = -25$ m, slightly in the lee of the sill. Note that for a time-dependent potential flow the location of the maximum fluid speed is independent of the time.

The horizontal pressure gradient p_x and the tangential pressure gradient $p_s = \hat{t} \cdot \nabla p$, where s is distance along the boundary, are shown at times $t = \tau/16$ and $t = \tau/4$ in figure 6*c, d*. At the latter time the flow is at maximum ebb and is not accelerating; hence, the pressure minimum along the sill occurs at $x = -25$ m, the location of maximum speed, as required by Bernoulli's equation. At the earlier time the flow is still accelerating to the right and both the horizontal and tangential pressure gradients are negative everywhere. There is no pressure minimum over the sill.

An illustrative analytic example, namely oscillating flow past a half-disc in an infinitely deep fluid, is presented in Appendix A. There it is shown that early during ebb flow there is no pressure minimum. As the flow increases in strength, a pressure minimum is eventually formed at the rightward (downstream) stagnation point, which thereafter moves upstream until it reaches the crest of the disc at the time of
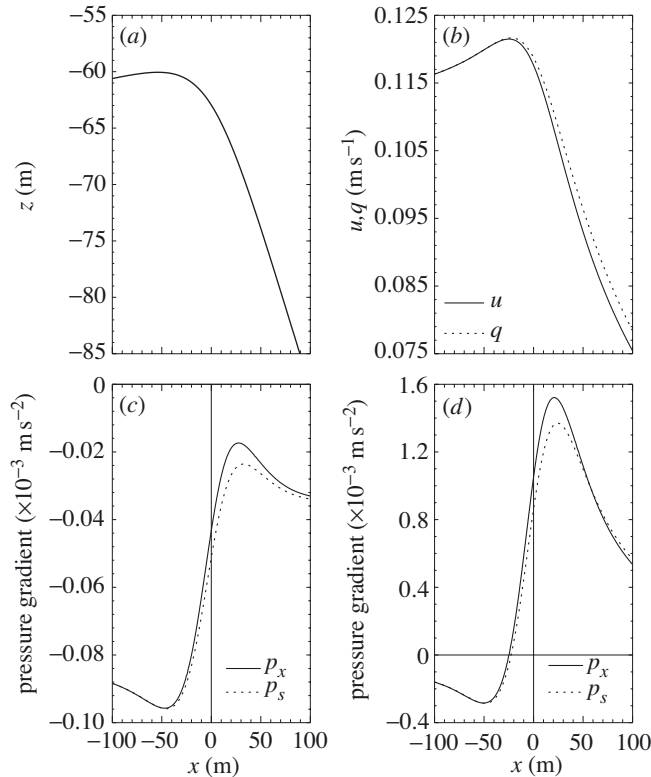
Figure 6. Potential flow over the sill. (*a*) Topography, (*b*) horizontal velocity (solid) and tangential velocity (dotted) along the lower boundary at $t = \tau/32 = 1395\ s$. Horizontal (solid) and tangential (dotted) pressure gradients along the lower boundary at (*c*) $t = \tau/32 = 1395$ s and (*d*) $t = \tau/4$ (peak ebb).

maximum flow. A similar process occurs for flow over the sill, with some important differences. Firstly, at maximum flow the pressure minimum is slightly downstream (for rightward flow) of the sill crest due to its asymmetric shape. Secondly, because of the variable curvature of the sill (as opposed to the constant curvature for a half-disc), a pressure minimum first appears well above the bottom of the sill. Indeed, from Bernoulli's equation for a time-dependent potential flow,

$$p_s = -q_t - qq_s, \tag{3.1}$$

is the tangential pressure gradient (recall that p has been scaled by the reference density). To separate the time dependence let

$$q = \sin(\omega t)r, \tag{3.2}$$

where r is independent of t. Then

$$p_s = -(\omega \cos(\omega t) + \sin^2(\omega t)r_s)r. \tag{3.3}$$

Since r is strictly positive along the bottom boundary, for small t the tangential pressure gradient p_s is negative everywhere. It first becomes zero at the location where r_s has its minimum (which is negative). The minimum of r_s occurs at $x = 29$ m

(close to where p_s has its maximum value in figure 6c, d). From (3.3) we find that the tangential pressure gradient first becomes zero at approximately $t = 1685$ s $(1.21\tau/32 = 0.038\tau)$. At earlier times the pressure gradient along the sill is favourable (pressure decreases in the direction of the flow). At later times, up to peak ebb flow, there is a section along the wall with an adverse pressure gradient.

The potential flow described above plays an important role in the evolution of the boundary layer in viscous flow over the sill because the flow outside the boundary layer is accurately modelled by the potential flow up to the time the flow first separates or when the boundary layer becomes too thick. In particular, the pressure field in the bottom boundary layer is set by this outer flow. Thickening of the boundary layer occurs most rapidly in the deep water downstream of the sill where fluid which has passed over the sill close to the bottom boundary is advected into the interior as streamlines separate. This process, however, does not strongly modify the flow over the sill.

Regions with an adverse pressure gradient play an important role in boundary-layer theory. For example, for a steady flow a region with an adverse pressure gradient is required for flow separation. For a viscous flow the curvature of the flow at the wall is determined by the sign of the tangential pressure gradient, since at a solid boundary the no-slip condition implies that

$$p_s = K u_{\eta\eta}, \tag{3.4}$$

where η is a coordinate perpendicular to the lower boundary. Under a favourable (adverse) pressure gradient, $u_{\eta\eta}$ has the opposite (same) sign as u_η at the boundary in regions where the flow above the wall is in the same direction as the outer potential flow. During ebb tide, potential theory predicts that the location and times for which an adverse pressure gradient exists are asymmetric about peak flow $(t = \tau/4)$ because $\cos(\omega t)$ is antisymmetric and $\sin^2(\omega t) r_s$ is symmetric about this time. In fact, between 0.41τ and 0.5τ there is an adverse pressure gradient everywhere over the sill.

Theoretical predictions of the time and location of initial flow separation $(u_\eta = 0$ at the wall) for a uniformly accelerating flow have been obtained by Blasius (1908) (see Schlichting 1979). For a potential flow with tangential flow $q = r(s)t$ along the boundary (starting from a state of rest at $t = 0$), the flow is predicted to separate at the first time that

$$1 + 0.427 \frac{\mathrm{d}r}{\mathrm{d}s} t^2 - 0.026 \left(\frac{\mathrm{d}r}{\mathrm{d}s} \right)^2 t^4 - 0.01 r \frac{\mathrm{d}^2 r}{\mathrm{d}s^2} t^4 = 0. \tag{3.5}$$

This prediction is independent of the viscosity. For the Knight Inlet sill, this equation predicts flow separation to occur at $x = 31$ m at $t = 2446$ s $(1.754\tau/32 = 0.055\tau)$. This is *ca.* 9 m below the sill crest. If the $O(t^4)$ terms are ignored, the flow is predicted to separate at $x = 29$ m at $t = 2579$ s $(1.862\tau/32 = 0.058\tau)$. Since the predicted time of separation is early during the tidal period, use of a constant flow acceleration is a good approximation to the actual sinusoidal flow.

Figure 7 shows some results from a model run with gravity set to zero but now with vertical viscosity and a no-slip bottom boundary condition (case B). As for the potential flow case, we use the density field as a tracer to illustrate fluid displacement (it is still subject to diffusion near the bottom). In this simulation the flow first separates ($u < 0$ one grid point above lower boundary) at $x = 70$ m at $t = 3100$ s.
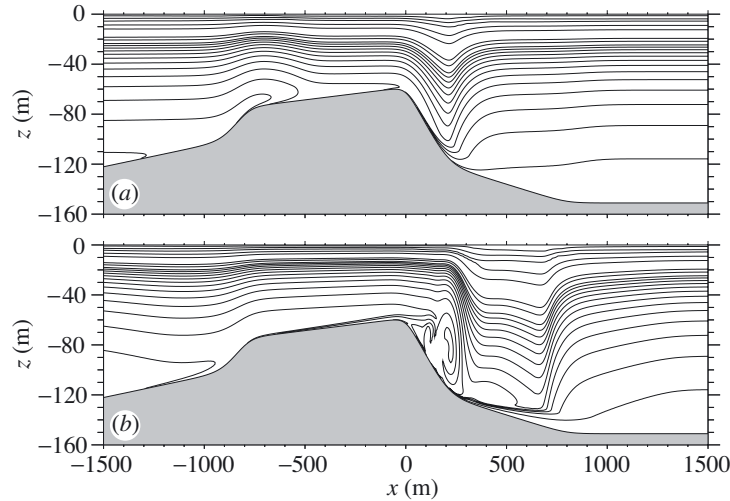
Figure 7. Unstratified flow over the sill with vertical viscosity/diffusivity given by equation (2.10) with $(C_u, C_\rho) = (0.02, 0.0002)$ m^2 s^{-1} and $\alpha = 0.25$ m^{-1}. $\Delta x = 1$ m. Case B. (*a*) $t = \tau/16$; (*b*) $t = \tau/8$.

This is 20 m below the sill crest. By $t = \tau/8 = 5580$ s the separation point has moved upstream to $x = 20$ m, *ca.* 7 m below the sill crest.

For this model run the resolution was 1 m in the horizontal (above the sill only) with 200 grid points in the vertical. In the model results, flow separation first occurs a distance below the sill equal to twice the theoretical prediction and at a slightly later time (3100 s against 2450 s). The theoretical prediction is of course an approximate theory, assuming, among other things, weak curvature of the bottom boundary. The discrepancy between the theoretical prediction and the model results must also be partly due to insufficient resolution in the bottom boundary layer. However, the separation point was not very different in a model run using d$x = 10$ m and with 100 grid points in the vertical.

The results discussed in this section have some important consequences for stratified flow over the sill. The potential flow solution illustrates that over the lee of the sill vertical displacement of fluid takes place throughout the water depth. As a consequence, waves are generated near the surface as well as near the bottom. While the largest vertical displacements occur near the bottom, it is not correct to view the waves as being generated at or near the bottom and subsequently propagating upward. While this phenomenon does occur, waves are also simultaneously generated near the surface. The relative importance of the various generation sites depends on the stratification (the body forcing term of Baines (1982)). In the extreme case of a two-layer fluid with the interface near the surface (as is approximately the case in Knight Inlet), small-amplitude waves are generated on the interface, due to the small vertical velocities present there. The generation of a lee wave is unavoidable in an inviscid model. The only possible way to inhibit lee-wave generation is to have boundary-layer separation from near the crest of the sill, and so substantially reduce the vertical component of the velocity field above the lee of the sill. The viscous results show, however, that boundary-layer separation does not occur until after $t = 2790$ s. Up to this time flow outside the bottom boundary layer is very similar
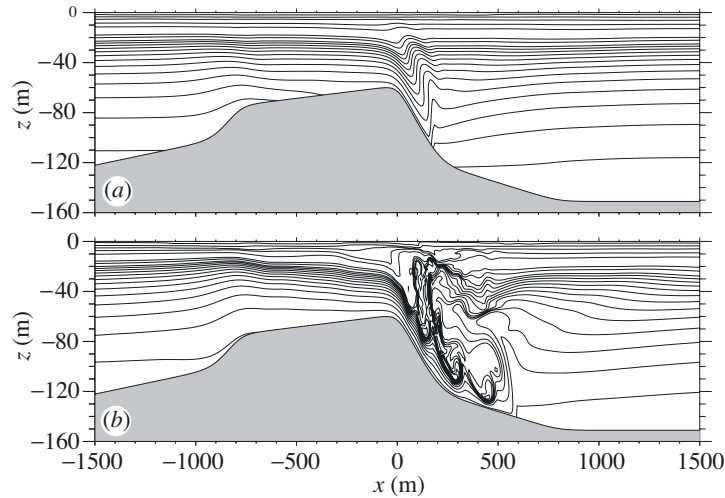
Figure 8. Density contours for case C. Inviscid model run without a deep water density pool. Values contoured were specified and are not at equal intervals. The same values are contoured for all figures. Horizontal resolution $\Delta x = 10$ m. (*a*) $t = \tau/16$; (*b*) $t = \tau/8$.

to the potential flow as can be seen by comparing figures 4*a* and 7*a*. These figures make it clear that, in the stratified cases, even the use of a no-slip bottom boundary condition to trigger flow separation will not eliminate the formation of a lee wave in model runs starting from rest.

4. The role of bottom boundary-layer separation and a deep salty pool on internal wave generation

In this section results from four stratified model runs are discussed. These runs were designed to investigate the relative importance of boundary-layer separation and of a cross-sill density jump on the evolution of the flow. These four cases demonstrate that boundary-layer separation is crucial for an accurate simulation of the flow over the Knight Inlet sill. They also demonstrate that a deep water density pool by itself is unable to cause flow separation but that it can enhance the separation of the bottom boundary layer.

Case C is an inviscid model run without a cross-sill density jump. Contour plots of the density field at $t = \tau/16 = 0.0625\tau$ and $\tau/8$ are shown in figure 8. Contour plots of the horizontal velocity field at $t = \tau/8$ and $3\tau/16 = 0.1875\tau$ are presented in figure 11. These illustrate the rapid establishment of a strong downslope jet. At $t = \tau/16$ a large lee wave has already developed slightly downstream of the crest. It extends right down to the bottom boundary (a depth of 100 m). By $3\tau/32 = 0.0937\tau$, overturning has commenced between depths of 20 and 90 m, i.e. virtually to the bottom, and a strong downslope flow has been established which extends downstream to about $x = 300$ m (not shown). By $\tau/8$, a high-drag state has formed. The downslope jet has strengthened, having a peak velocity of *ca.* 1.0 m s^{-1}, and it now extends downstream to about $x = 600$ m, where it ends in a hydraulic jump (see figure 11). As the flow evolves, the *ca.* 40 m thick jet lengthens as the hydraulic jump moves downstream. Above is a thick layer of slow-moving fluid. Instabilities can be
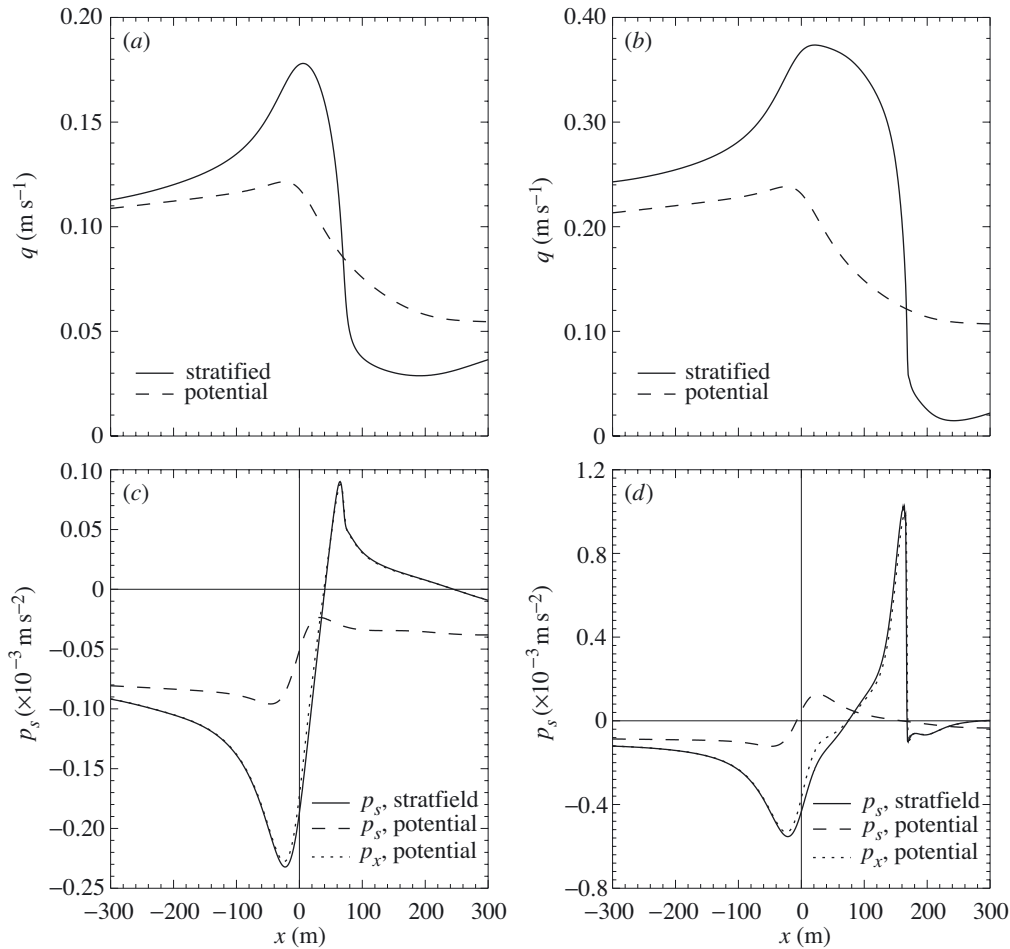
Figure 9. Comparison of potential flow (case A) with stratified inviscid flow (case C). Tangential flow along the lower boundary at (*a*) $t = 1395$ and (*b*) $t = 2790$ s. Tangential and horizontal pressure gradients along the lower boundary at (*c*) $t = 1395$ and (*d*) $t = 2790$ s.

seen in the downslope jet starting at about $\tau/8$. These have been extensively studied in the atmospheric context (e.g. Scinocca & Peltier 1989; Afanasyev & Peltier 2001*a*, and references therein).

Before considering the next case, which uses vertical viscosity/diffusivity, we briefly compare the stratified and unstratified inviscid model runs. Comparison of figures 4*a* and 8*a* show that gravitational adjustment has resulted in a substantial narrowing and deepening of the depression in the lee of the sill. By $t = 2790$ s the depression is about half the width in the stratified case, a reflection of the upstream propagation of the depression (some of the depression propagates down stream). In figure 9*a, b* the tangential component of the velocity along the bottom boundary for case A is compared with the potential flow at times $t = 1395$ and 2790 s. For the stratified case q is substantially larger than in the unstratified case over and slightly downstream of the sill. This is a consequence of the positive bottom velocities associated with the leftward-propagating wave of depression. At the back of the wave this velocity per-
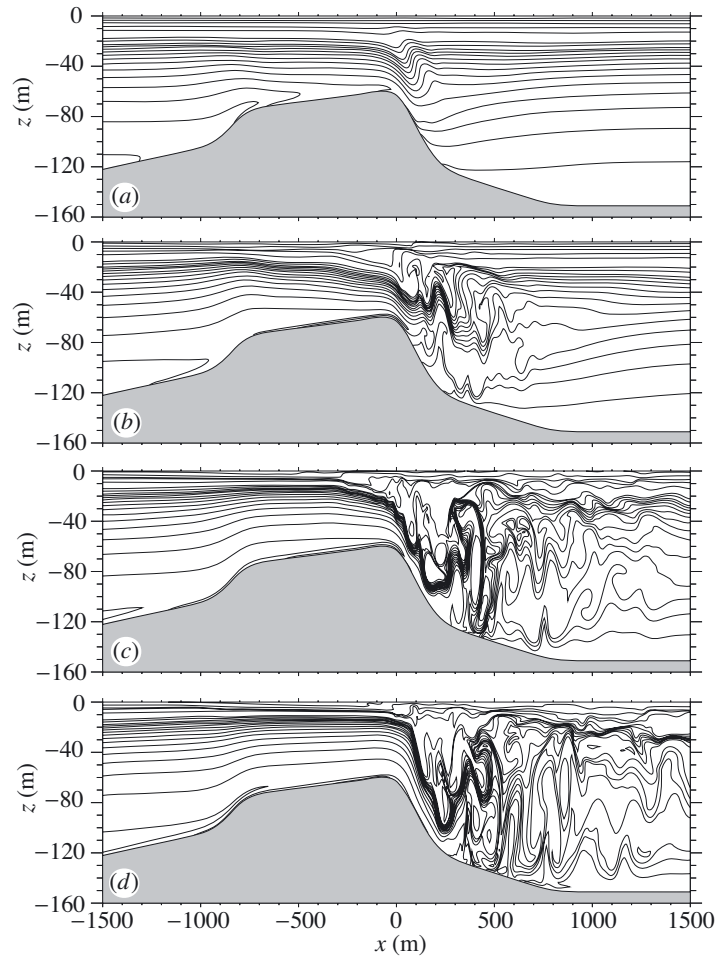
Figure 10. Density contours for case D. Vertical viscosity/diffusivity given by (2.10) with $(C_u, C_\rho) = (0.02, 0.0002)$ m^2 s^{-1} and $\alpha = 0.25$ m^{-1}. $\Delta x = 10$ m. No density pool. (*a*) $t = \tau/16$; (*b*) $t = \tau/8$; (*c*) $t = 3\tau/16$; (*d*) $t = \tau/4$.

turbation drops rapidly and becomes negative (hence $q_{\mathrm{strat}} < q_{\mathrm{potential}}$). Figure 9*c*, *d* shows the tangential pressure gradient p_s at the same times. Here, the hydrostatic part of the pressure gradient has been removed for the stratified case and hence $p_s = \hat{t} \cdot (\nabla p + g\rho\hat{k})$. Also shown is the horizontal pressure gradient p_x for the stratified case. It is very similar to p_s. At $t = 1395$ s, $p_s < 0$ everywhere for the potential flow solution, and hence the pressure gradient is favourable over the sill. For the stratified case, however, p_s is positive between $x = 40$ and 260 m. This is associated with the rapid drop in q in the rear half of the leftward-propagating depression wave. At $t = 2790$ s, p_s is an order of magnitude larger in the rear of the wave.

Because of the adverse pressure gradients created by the wave we can expect that in the model runs with vertical viscosity, boundary-layer separation will occur earlier in the stratified case than in the unstratified case. This indeed turns out to be the case.
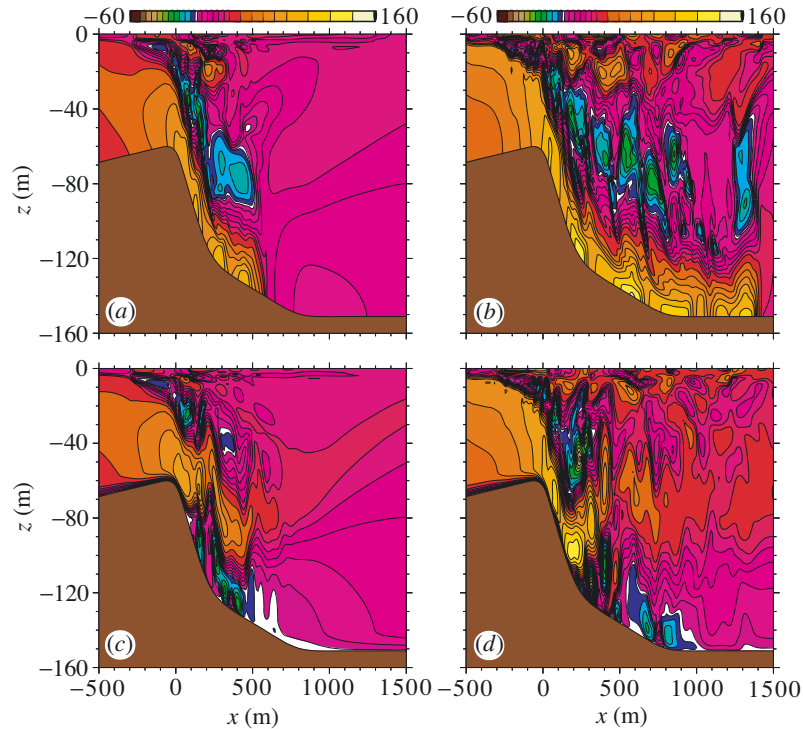
Figure 11. Contour plots of the horizontal velocity. Case C (inviscid, stratified flow) at (*a*) $t = \tau/8$ and (*b*) $t = 3\tau/16$. Case D (viscous, stratified flow) at (*c*) $t = \tau/8$ and (*d*) $t = 3\tau/16$. Block sizes in colour bar are 5, 10 and 20 cm s^{-1}. Values between ± 0.01 m s^{-1} are in white.

Case D uses a vertical eddy viscosity/diffusivity with a no-slip bottom boundary condition with $(C_u, C_\rho) = (0.02, 0.0002)$ m^2 s^{-1}. Values of K_u and K_ρ have these maximum values at the bottom boundary and decrease above the bottom with an inverse scale height of $\alpha = 0.25$ m^{-1} (see figure 3). Density contour plots are shown in figure 10 at four different times. Contour plots of u are given in figure 11. Some significant differences between cases C and D are apparent. Prior to the onset of flow separation, downward flow in the lee of the sill has been reduced below the sill crest. As a consequence, vertical displacements of fluid are reduced and consequently the lee wave formed downstream of the sill is greatly reduced in amplitude. Flow separation below the sill crest occurs *ca.* 25 m below the top of the sill starting at about $t = 3700$ s. This should be compared with the unstratified case (case B) for which flow separation occurred earlier (at $t = 3100s$) 20 m below the sill crest. The delay in separation and the slightly deeper depth can be attributed to the enhanced bottom flow near the bottom associated with the rightward-propagating wave of depression. This instance of flow separation is not the first, however. Flow separation first occurs at a much greater depth ($x = 250$ m, 80 m below the sill crest) at about $t = \tau/16 = 2790$ s, behind the leftward-propagating wave of depression.

By $3\tau/32 = 0.09375\tau$ the developing lee wave has commenced overturning but only in the upper 50 m (not shown). In contrast, at the same time in the inviscid run (case C) overturning occurs to a depth of *ca.* 90 m. By $t = \tau/8$ the flow separation point has moved up slightly, breaking in the large lee wave is confined to the upper
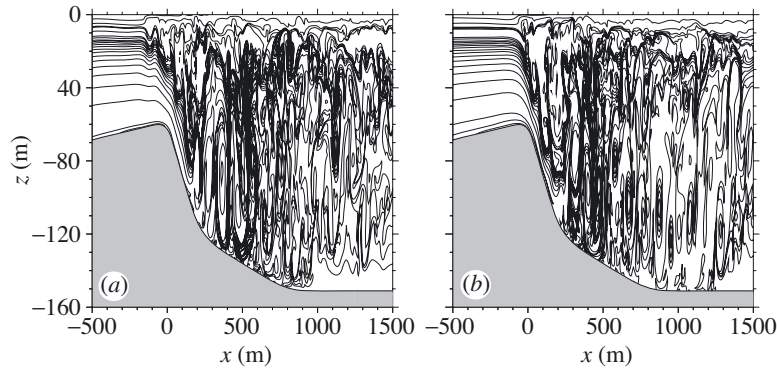
Figure 12. Contour plots from a rerun of case D using higher horizontal resolution of $\Delta x = 2.5$ m (case J). (a) $t = \tau/4$; (b) $t = 3\tau/8$.

40 m, and the reverse flow under the flow separation line has strengthened. At this stage in the inviscid model run, a high-drag state has already been reached with a strong, unstable downslope jet. Between $\tau/8$ and $3\tau/16$ the lee wave grows rapidly and the flow separation point moves to a depth of 110 m. Thereafter, the lee wave grows more slowly and the separation point slowly moves deeper. It has a depth of 120 m at peak ebb ($t = \tau/4$). Although a strong down-slope jet is formed down the sill slope, it terminates just behind the deep trough of the lee wave in a hydraulic jump. This is known as post-wave separation (Baines 1995). This is clearly seen in the contour plots of the horizontal velocity shown in figure 11. At $t = \tau/4$, downstream of the separation point the flow is seaward throughout most of the water column, the exception being a weak reverse flow near the bottom. In contrast, in the inviscid model run, the downslope jet extends beyond 1500 m. It is *ca.* 40 m thick with large positive velocities in a layer *ca.* 15–20 m thick. Above lies a layer of weak reverse flow between 40 and 90 m above the bottom. Peak horizontal velocities are smaller in case D (1.2 against 1.8 m s^{-1} at $t = \tau/4$).

For approximately the first eighth of the tidal period, mode-2 waves launched at the lee of the sill can propagate upstream over the sill. A mode-2 wavefront can be seen in figure 10. It is at *ca.* $x = -300$ m at $t = \tau/8$. As the tidal current strengthens, it is swept downstream to near the sill crest. At peak ebb tide a hydraulic control point has been established at this point. The precise location of the control point is somewhat sensitive to the form of the vertical viscosity/diffusivity and to the model resolution. Cases C and D used a horizontal resolution of 10 m. Case D was rerun using a horizontal resolution of 2.5 m (case J, see below). Mode-2 solitary waves, which have a propagation speed greater than the linear long-wave propagation speed, were generated. At $t = \tau/4$ the leading one was *ca.* 100 m ahead of the location of the control point for case D. At this time the solitary waves were advected downstream and by $t = 3\tau/8$ no waves lay upstream of the control point, which is near $x = 0$. This is shown in figure 12. The early stages of flow development were not significantly changed by the increased resolution. Downstream of the sill the details of the flow rapidly became quite different after the lee wave overturns. These affected the amplitudes of lee waves downstream of the sill, which in turn influenced the location of the flow separation and reattachment points. Three-dimensionalization of the flow would also be expected to modify the flow downstream
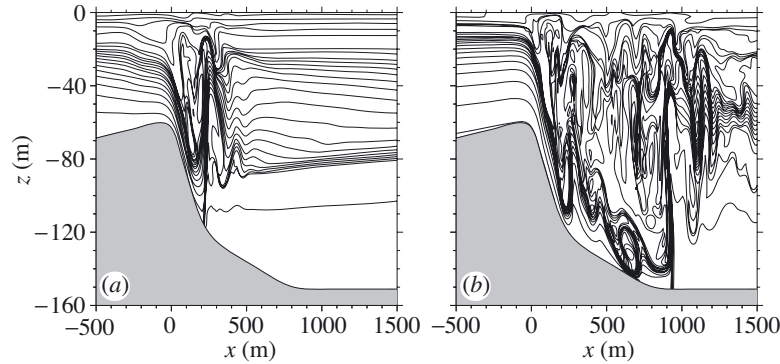
Figure 13. Density contours for case E: density pool, no viscosity/diffusivity.
$\Delta x = 10$ m. (*a*) $t = \tau/8$; (*b*) $t = \tau/4$.
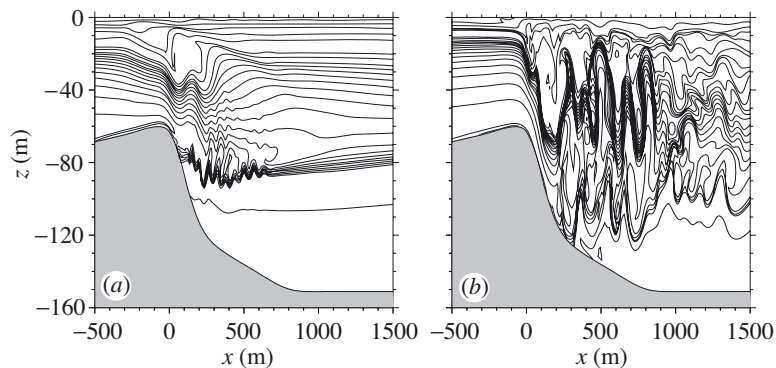

Figure 14. Density contours for case F: density pool, vertical viscosity/diffusivity
as in figure 10. $\Delta x = 10$ m. (*a*) $t = \tau/8$; (*b*) $t = \tau/4$.

of the sill. For the higher-resolution run the separation point started moving down slightly earlier and its final depth was *ca.* 10 m shallower and exhibited a little more variability.

Huppert & Britter (1982) showed that for hydrostatic flow of one- and two-layer fluids, flow separation occurs if the flow is subcritical everywhere, and the flow remains attached if it is supercritical but it separates at a hydraulic jump. The above results are consistent with their findings. Flow separation occurs early in a ebb tide, when the flow is subcritical everywhere. In the high-drag state, for which the jet of fluid is supercritical, the boundary layer remains attached until immediately behind the large lee wave, where it separates from the lower boundary in a hydraulic jump.

The observations of Klymak & Gregg (2003) show that there is a density difference across the sill, with water on the seaward side being 0.5 kg m^3 denser at depths below the sill. The density contrast extended well above the sill. They have suggested that the denser water on the seaward side of the sill is an important contributing factor to flow separation. To explore this possibility several model runs were done using a horizontally varying density. Results from two cases, with and without vertical viscosity/diffusivity, are presented in figures 13 and 14. For these cases the density is
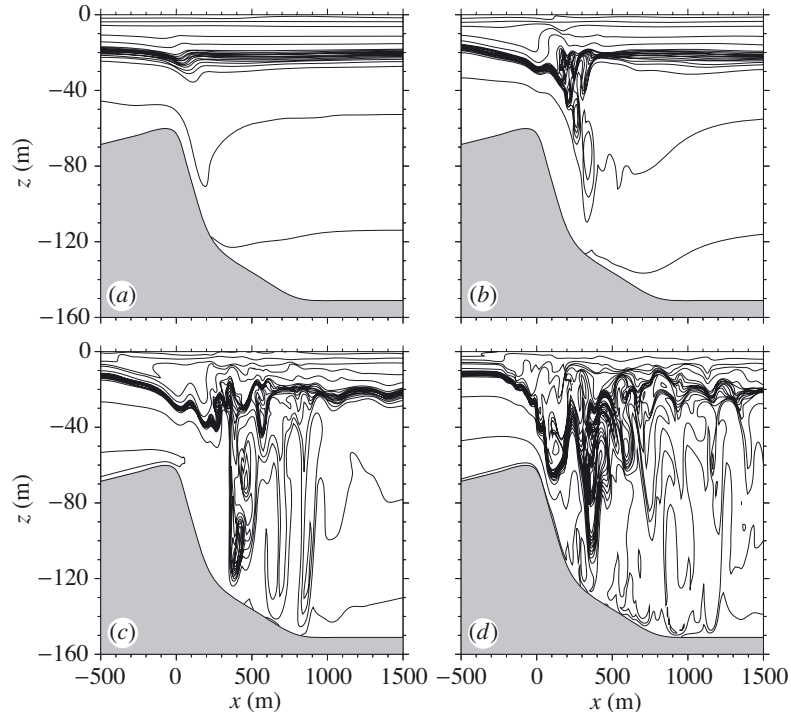
Figure 15. Density contours for case G: density $\bar{\rho}_3(z)$, same viscosity/diffusivity as for case D (figure 10). $\Delta x = 10$ m. (*a*) $t = \tau/16$; (*b*) $t = \tau/8$; (*c*) $t = 3\tau/16$; (*d*) $t = \tau/4$.

increased by 0.5 kg m^3 seaward of the sill below the sill top. This is done by adding

$$\Delta\rho = 0.25\left(1 - \tanh\left(\frac{z+60}{5.0}\right)\right)H(x) \qquad (4.1)$$

to the density, where $H(x)$ is the Heaviside step function equal to zero for $x < 0$ and unity for $x \geqslant 0$. Some model runs were done with an initial density field that had a horizontal density variation extending above the sill. Results using such a horizontally varying stratification for a different base density are presented in §4 *c*. For the base density $\bar{\rho}_1$ used here, the results obtained using a horizontal density variation extending above the sill crest did not differ qualitatively from those presented in figures 13 and 14.

For the inviscid model run (case E), the presence of the deep-water density pool significantly decreases the amplitude of the lee wave during its early stages ($t \leqslant 3\tau/32 = 0.09375\tau$). However, the deep-water density pool is ultimately pushed away from the sill and by $t = \tau/8$ the overturning lee wave extends to the same depth as in case C upstream of the density front ($x = 200$ m). Thereafter the flow is similar for the two cases upstream of the density front, which continues to move downstream (figure 13).

Case F differs from case E only in the use of a vertical viscosity/diffusivity which is the same as that used in case D. Of the four cases considered thus far, this case has the smallest lee wave during the early stages of the flow development. At $t = 3\tau/32 = 0.09375\tau$ overturning has just commenced in the upper 30 m, compared with
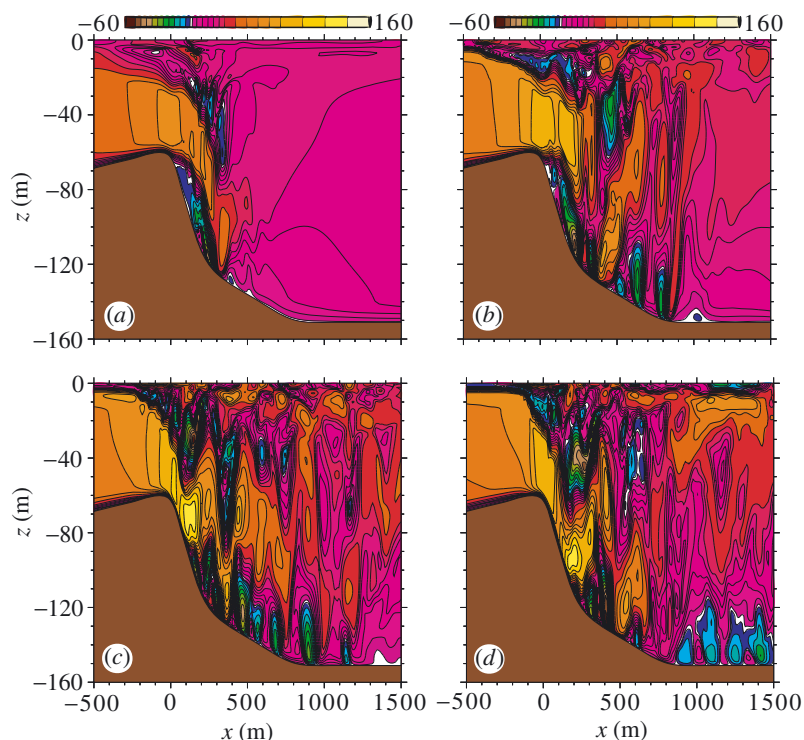
Figure 16. Horizontal velocity for case G. (*a*) $t = \tau/8$; (*b*) $t = 3\tau/16$; (*c*) $t = \tau/4$; (*d*) $t = 3\tau/8$.

the upper 50 m for case D. At $t = \tau/8$ the flow separation point is at its shallowest among the four cases, being *ca.* 10 m below the sill top. As the flow evolves, the region of slow-moving fluid formed by the overturning lee wave deepens and the separation point moves down the sill. The leading lee wave that is formed is considerably smaller than in Case D. By $t = \tau/4$, post-wave separation occurs at a depth of *ca.* 100 m, 20 m higher than in case D. The deep-water density pool is not pushed beyond this point, in contrast to the inviscid run.

5. Sensitivity studies

The sensitivity of the results presented in the preceding section to the background density field and the eddy viscosity/diffusivity parametrization are now considered. For reasons of computational efficiency, the majority of the model runs were done starting from a quiescent state at the beginning of ebb tide. In nature, however, an ebb tide is but one of a continual cycle of ebb and flood tides. Two model runs were done to investigate the effects of a preceding flood tide on the formation of the lee wave and on the evolution of the boundary-layer separation.

(*a*) *Sensitivity to initial density field*

We first explore the sensitivity of the results to the initial density profile. Density $\bar{\rho}_2$, given by (2.7), was used for values of z_0 between -20 and -5 m and for values of d between 7.5 and 2.5 m. All these model runs differed considerably from case D. The

results were found to be most sensitive to changes in the stratification immediately above the sill. Thus, we illustrate the sensitivity to the stratification immediately above the sill by showing some model results from case G which uses density $\bar{\rho}_3(z)$ given by (2.8). This density is identical to density $\bar{\rho}_1(z)$ near the surface but has a reduced stratification at depths greater than 20 m. Results from this case are presented in figures 15 and 16. This case is identical to case D except for the change in density.

Reducing the strength of the stratification below a depth of 20 m significantly reduces the amplitude of the lee wave. It breaks later and the initial overturning is confined to the upper 30 m. As a result there is a delay in the downward movement of the separation point. In case G the separation at early times is *ca.* 10 m below the sill crest, as opposed to *ca.* 25 m for case D. By $t = 3\tau/16 = 0.1875\tau$ the separation point has not moved down in case G, while in Case D it was at a depth of *ca.* 110 m (see figure 10). At peak tidal flow the separation point has shifted to a depth of 90 m and by $t = 5\tau/16 = 0.3125\tau$ it has reached a depth of 110 m. At this point a high-drag state has been formed with post-wave separation. The separation point remains at this depth for almost the duration of the ebb flow, having risen to a depth of 100 m at the end of ebb flow. The observations of FA99 also showed a similar persistence of the high-drag state once formed. The delay in the downward movement of the separation point, relative to case D, can be attributed to the slower growth and reduced amplitude of the lee wave. This reduces the strength of the high-pressure region needed to push the separation point down.

(b) *Sensitivity to eddy viscosity/diffusivity*

The sensitivity of the results to the vertical eddy viscosity/diffusivity was also investigated. First, the value of α was varied. Doubling or halving α did not result in significant changes in the model results. However, setting α to zero, which gives a (large) vertically uniform eddy viscosity/diffusivity, resulted in a flow separation which lasted the whole of ebb tide. The vertical viscosity/diffusivity (2.10) was also augmented by the Richardson-number-based parametrization of Pacanowski & Philander (1981), modified to include a cut-off value. This parametrization (henceforth referred to as the PP parametrization) has

$$K_h = \begin{cases} \dfrac{\beta_h}{(1 + 5Ri)^2} + \gamma_h, & \text{if } Ri > -0.1, \\ 4\beta_h + \gamma_h, & \text{if } Ri < -0.1, \end{cases} \tag{5.1}$$

added to the eddy viscosity, and

$$K_m = \begin{cases} K_h(1 + 5Ri) + \gamma_m, & \text{if } Ri > -0.1, \\ 0.5K_h + \gamma_m, & \text{if } Ri < -0.1, \end{cases} \tag{5.2}$$

added to the vertical eddy diffusivity.

It is unclear which values of β_h, γ_h and γ_m are most suitable for the present situation, or indeed whether the parametrization given by (5.1) and (5.2) is a good choice. It is used here solely to demonstrate the sensitivity of the model results. Given the energetic environment it seems reasonable to focus on larger values of β_h.

Case H is identical to case G except for the use of the PP parametrization using $\beta_h = 5 \times 10^{-2}\,\mathrm{m^2\,s^{-1}}$, and $\gamma_h = \gamma_m = 10^{-5}\,\mathrm{m^2\,s^{-1}}$. These parameter values give a maximum of K_h equal to $0.2/0.05\,\mathrm{m^2\,s^{-1}}$ in overturning/non-overturning regions. As a comparison, Cummins (2000) shows a plot of the eddy diffusivities calculated by the Mellor–Yamada turbulence closure in the POM. Four hours into ebb tide the vertical eddy viscosities above and in the lee of the sill range from 0.01 to over $10\,\mathrm{m^2\,s^{-1}}$, the largest values being in the large breaking lee wave above the sill crest.

Density contours for case H are shown in figure 17. Comparing the results with those from case G we find that the lee-wave amplitude is significantly reduced, the separation point is 5 m below the sill crest (as opposed to 95 m) at $t = \tau/4$, and that the separation point reaches a maximum depth of 90 m well after peak tide. A train of lee waves can be seen at $t = \tau/4$. Similar wave trains have been observed at the Knight Inlet sill (Farmer & Freeland 1983, fig. 19).

In a model run with the vertical eddy diffusivity reduced by about a factor of 10, the lee wave did not grow and the separation point did not move down the lee of the sill. This supports the idea, put forth by FA99, that mixing into the nearly stagnant fluid plays an important role in determining the growth rate of the lee wave. However, given the ad hoc parametrization used here, further investigation is required.

(c) Combined effect of modified density, deep water density pool and PP parametrization

We now consider a model run (case I) which differs from case H by the addition of a deep water density pool on the seaward side of the sill. In particular, the initial horizontally varying density field is given by

$$\bar{\rho}_4(x, z) = \bar{\rho}_3(x, z) + 0.125\left(1 + \tanh\left(\frac{x + 400}{400}\right)\right)\left(1 - \tan\left(\frac{z + 45}{5.0}\right)\right). \quad (5.3)$$

In contrast to case F, the density increase on the seaward side of the sill now extends 15 m above and 400 m to the landward side of the sill crest. In comparison with case D, case I has reduced stratification below the pycnocline, a deep water density pool extending above the sill crest and has eddy viscosity/diffusivity parametrization in the flow interior.

Results are shown in figure 18. They are quite different from earlier results. A large lee wave never forms. In its place, a train of small-amplitude lee waves, *ca.* 5 m in amplitude, is formed. At $t = \tau/4$ the leading-wave is slightly downstream of the sill crest and is being advected downstream. It reaches its greatest downstream distance of *ca.* 200 m at $t = 5\tau/16 = 0.3125\tau$. In conjunction with these small-amplitude lee waves, flow separation occurs less than 5 m below the sill crest throughout ebb tide. The shear layer associated with the flow separation is unstable, as indicated by the large amplitude waves on the shear layer downstream of the sill.

A model run with β_h reduced by a factor of 10 to 5×10^{-3} gave similar results. At about $t = 5\tau/16$ a lee wave started to form over the lee of the sill. It reached a peak amplitude of *ca.* 40 m at $t = 13\tau/32 = 0.40625\tau$. At this time the separation point (post-wave) was *ca.* 15 m below the sill crest. Other differences between the two runs included larger waves in the shear layer associated with the flow separation. This resulted in pulsations in the flow below the shear layer which occasionally resulted in a series of reattachment and post-wave separation points.
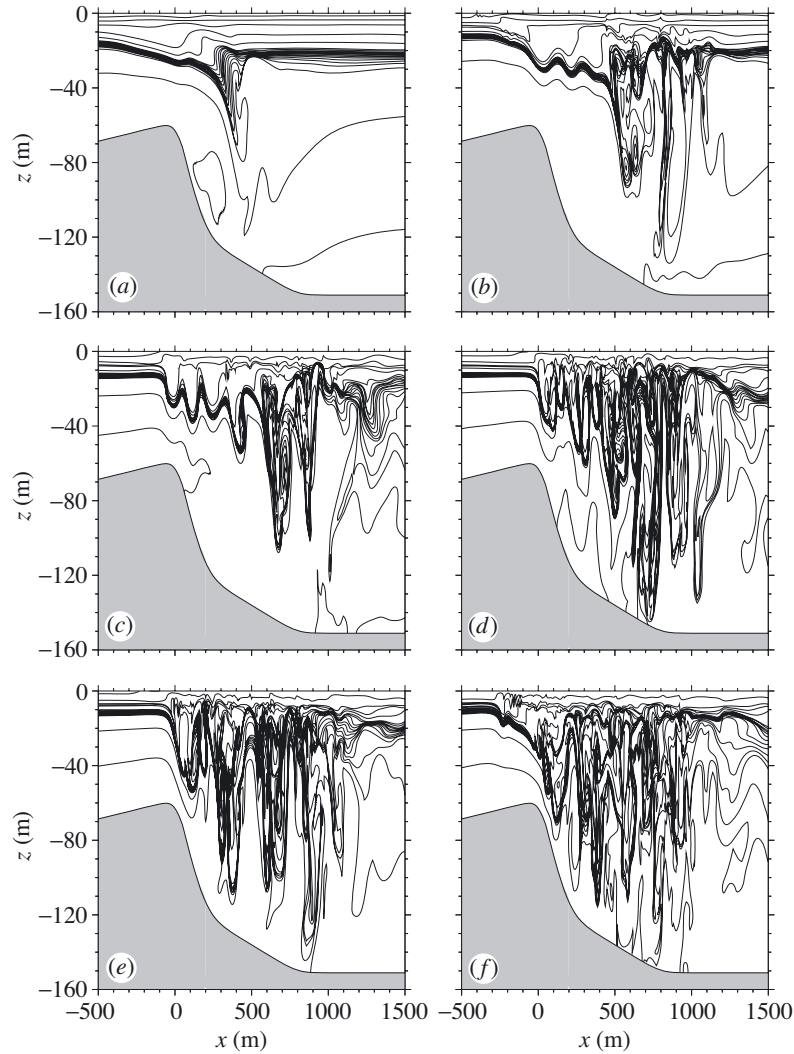
Figure 17. Density contours for case H. Same as case G but with PP parametrization using $\beta_h = 5 \times 10^{-2}\ \mathrm{m^2\ s^{-1}}$, and $\gamma_h = \gamma_m = 10^{-5}\ \mathrm{m^2\ s^{-1}}$. $\Delta x = 10$ m. Every sixteenth of a tidal period from $t = \tau/8$ to $t = 7\tau/16$.

An inviscid model run with the same initial density field gave results qualitatively similar to case E in that a large lee wave and a strong downslope jet terminating in an hydraulic jump were rapidly formed.

(d) *The effect of a preceding flood tide*

A few longer models runs were done. Case J was similar to case D except that it was run for 1.5τ and had a horizontal resolution of 2.5 m. In figure 19 some vertical density and horizontal velocity profiles are shown from locations taken every 50 m between $x = -300$ m and $x = 0$ after one tidal period. These show that after one tidal period the strength of the pycnocline has been reduced and that there is considerable
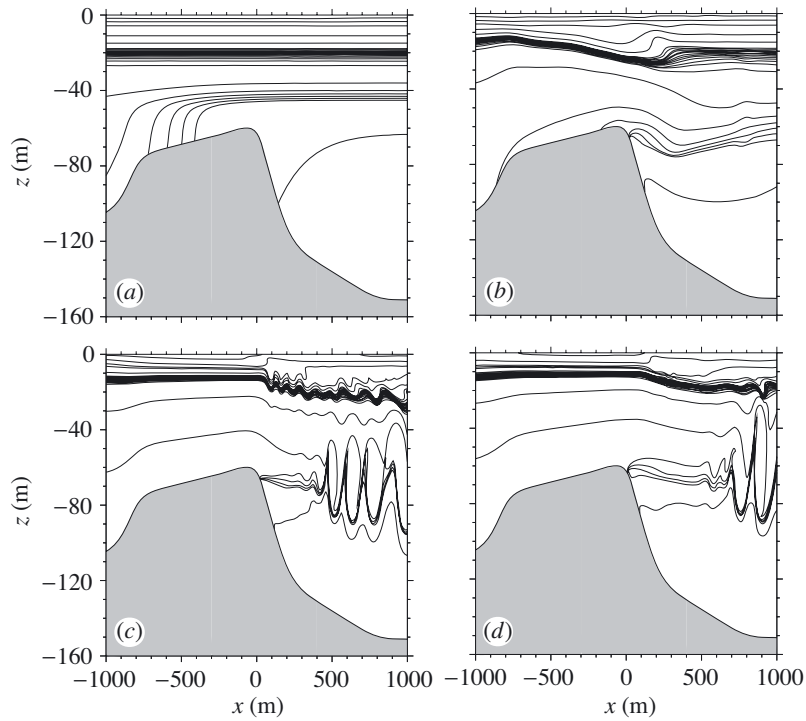
Figure 18. Density contours for case I. Density $\bar{\rho}_4(z)$. PP parametrization. This model uses $\beta_h = 5 \times 10^{-2}$ m^2 s^{-1} and $\gamma_h = \gamma_m = 10^{-5}$ m^2 s^{-1}. $\Delta x = 10$ m. (a) $t = 0$; (b) $t = \tau/8$; (c) $t = \tau/4$; (d) $t = 3\tau/8$.
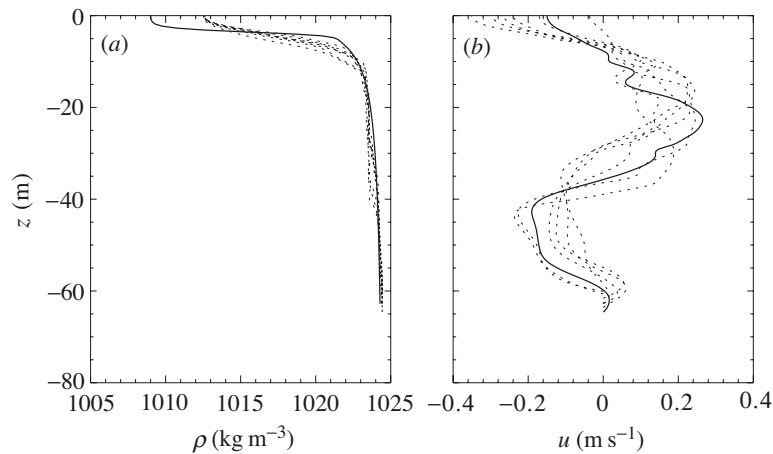

Figure 19. Vertical profiles of density and horizontal velocity fields after flood tide ($t = \tau$) for case J. (a) Density profiles. Solid curve is initial density. Dotted curves are density profiles every 50 m between $x = -300$ m and $x = 0$. (b) Horizontal density profiles. Solid curve is horizontal velocity profile at $x = 0$. Dotted curves are profiles every 50 m between $x = -300$ and $x = -50$ m.
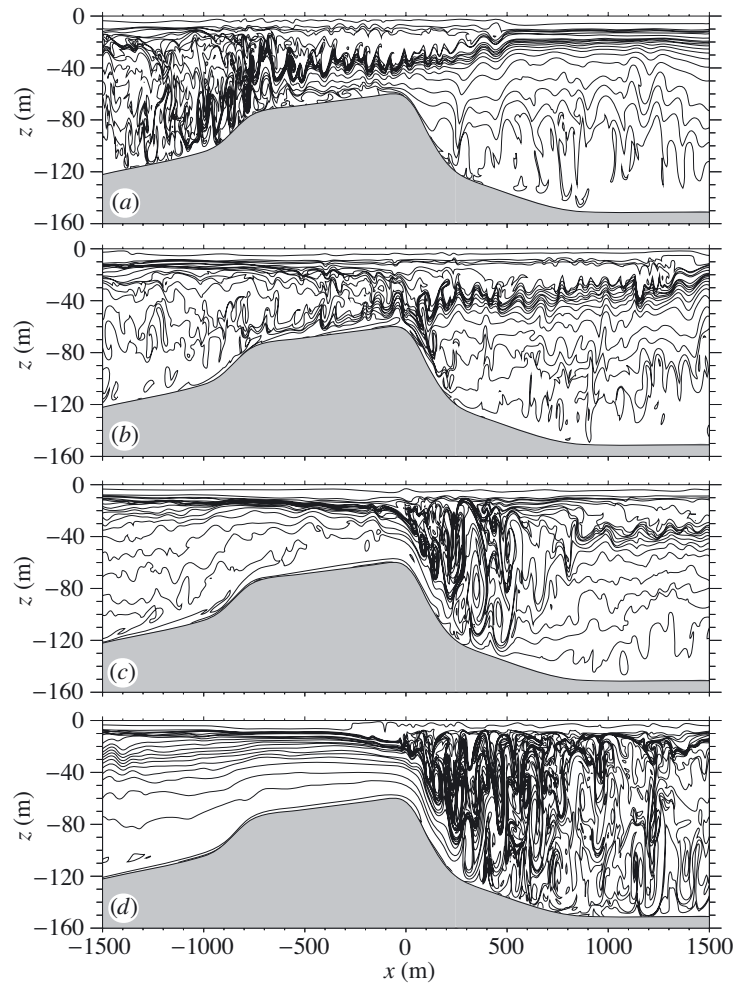
Figure 20. Density contours for case J starting at end of flood. Density $\bar{\rho}_1(z)$.
$\Delta x = 2.5$ m. (a) $t = \tau$; (b) $t = 17\tau/16$; (c) $t = 9\tau/8$; (d) $t = 5\tau/4$.

vertical structure to the velocity field. The velocity profiles show a pronounced mode-2 structure. Flow is seaward (positive) between depths of $ca.\,10$ and 30–40 m. Flow is landward above and below these depths, apart from a small region in the bottom boundary layer. The peak velocities are a significant fraction of the peak barotropic tidal current over the sill. The observations reported in FA99 give no indication of such a current structure near the start of ebb tide. In the model results these currents are associated with the passage of a large amplitude mode-2 bore generated during flood tide. This is shown in figure 20. At $t = \tau$, the front of the seaward-propagating bore is at $x = 500$ m. A series of overturning waves on the shear layer beneath the bore (at depths of $ca.\,40$ m) are readily apparent, indicating that the sheared flow associated with the bore is unstable.

By $t = 5\tau/4$, at peak ebb tide, the flow over the sill is laminar. A large lee wave has formed over the lee of the sill, very similar to that in case D. The preceding ebb
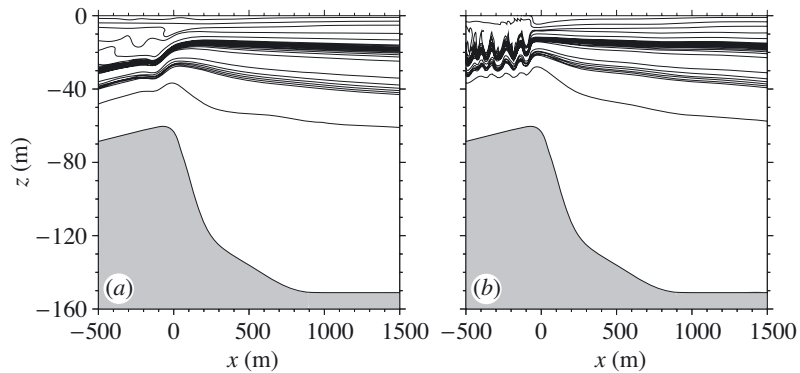
Figure 21. Density contours for case K during flood tide. Density $\bar{\rho}_4(z)$. Uses PP parametrization using $\beta_h = 5 \times 10^{-3}$ m^2 s^{-1} and $\gamma_h = \gamma_m = 10^{-5}$ m^2 s^{-1}. $\Delta x = 2$ m. (a) $t = \tau/8$; (b) $t = \tau/4$.
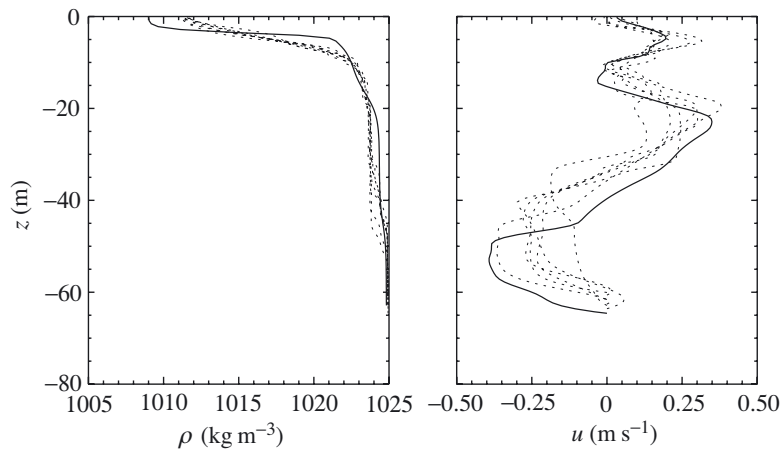

Figure 22. Vertical profiles of density and horizontal velocity fields after flood tide ($t = 0.5\tau$) for case K. Curves as for figure 19.

and flood tides do not appear to have had a significant impact on the nature of the flow at this time.

We next consider case K which uses the same horizontally varying density (5.3) used in case I. The PP parametrization was used with $\beta_h = 5 \times 10^{-3}$ m^2 s^{-1} (a factor of 10 smaller than in case I) and $\gamma_h = \gamma_m = 1 \times 10^{-5}$ m^2 s^{-1}. The model run started at the beginning of flood tide and was run for one tidal period. Contour plots during flood tide are shown in figure 21. Figure 22 shows some vertical density and horizontal velocity profiles at the end of flood tide. At the end of flood tide the near-surface density gradient has been reduced. The vertical structure of the horizontal velocity is more complicated than in the preceding case. It is positive in the upper 30–45 m with two velocity maximums. Flow is landward at greater depths, except for some small positive velocities in the bottom boundary layer. The directions of these flows are consistent with an exchange flow driven by the density difference across the sill. Note the larger near-bottom negative velocities ($ca. -0.4$ m s^{-1}) than in the previous case.

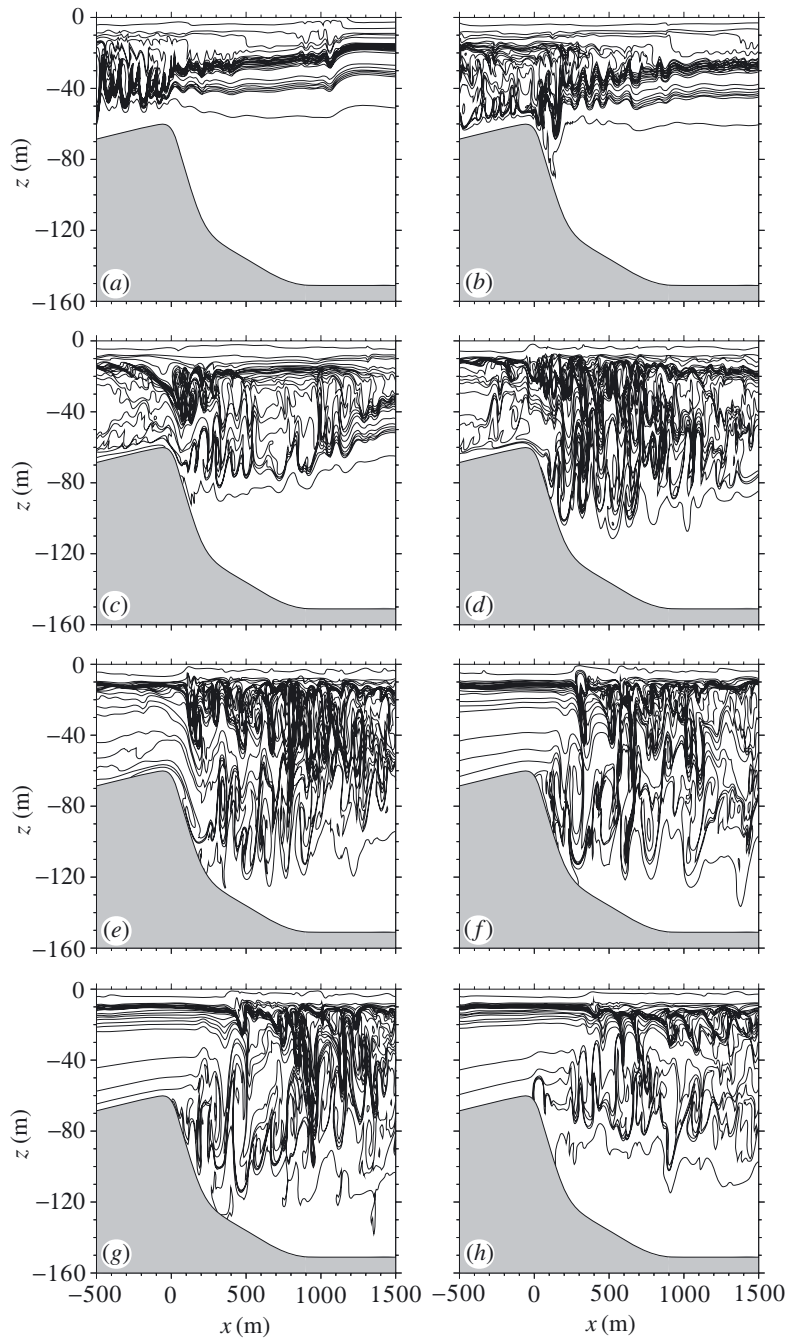Figure 23. Density contours for case K during ebb tide. Every sixteenth
of a tidal period from $t = \tau/2$ to $t = 15\tau/16$.

During ebb tide a lee wave has formed by $t = 5\tau/8$ (figure 23). In contrast, in a model run using the same PP parametrization and initial density, but beginning at the start of ebb tide, a large lee wave was not formed until $t = 3\tau/8$, much later into ebb tide. In both cases a small broad lee wave is formed early in ebb tide. Only in the model run which started at the beginning of flood tide does this wave grow significantly in the first half of ebb tide. Differences in the initial density and velocity fields at the start of ebb tide could account for this difference. Another possible mechanism for the growth of the wave is the enhanced vertical mixing caused by the strongly sheared flow at the end of flood tide. A model run continued from the end of flood tide with the PP parametrization turned off produced similar results, making this mechanism doubtful.

The lee wave is sporadic. At $t = 11\tau/16 = 0.6875\tau$ it is greatly reduced in size but has reappeared at $t = 3\tau/4$. At this time the flow separates *ca.* 40 m below the sill crest. The lee wave is thereafter advected downstream and the flow above the sill crest is laminar as far as 400 m downstream of the sill crest. In conjunction, the flow separates from the sill crest for the remainder of ebb tide, similar to the late stages of ebb tide for case I.

6. Discussion and summary

In all but one of the model runs presented in the preceding sections, a large lee wave is generated. The lee wave grows in time, breaks, and the resulting patch of slow-moving fluid forms the high-pressure region required to create the high-drag state associated with the fast moving, downslope jet of fluid beneath the breaking wave. Boundary-layer separation significantly modifies the evolution to the high-drag state by delaying it and limiting the downstream extent of the jet, which always leaves the topography immediately behind the lee wave.

The field observations of FA99 (see their figure 7) suggest that the transition to a high-drag state occurs shortly after peak ebb tide. For the base model run using the observed density, with no density pool and without the PP parametrization (case D), the transition to the high-drag state occurs much earlier, shortly after an eighth of a tidal period. Other model runs showed, however, that the transition to a high-drag state can be delayed further when: the stratification immediately above the sill is weakened (case G, figures 15 and 16); the viscosity/diffusivity terms are increased outside of the bottom boundary layer (case H, figure 17); and a deep water density pool is added on the seaward side of the sill (case F, figure 14 and case I, figure 18). In case I, in which all three of these affects are present, a high-drag state is never formed. These results indicate a considerable sensitivity to the details of the model. On the one hand this is encouraging given the rich variety of flows observed over the Knight Inlet sill (Farmer & Smith 1980; Farmer & Freeland 1983; FA99). On the other hand, it suggests that an accurate simulation of an observed flow will be very difficult, particularly as the sensitivity of the model results to the stratification, viscosity/diffusivity parametrization and horizontal inhomogeneities implies a sensitivity to 3D features of the topography and of the flow.

One model run, case H, provided some support for FA99's contention that mixing of fluid into a slow-moving, near-surface wedge of fluid can lead to growth of the lee wave. This model run used density $\bar{\rho}_3(z)$, for which the strength of the stratification below a depth of 20 m was reduced from the observed stratification. It also used
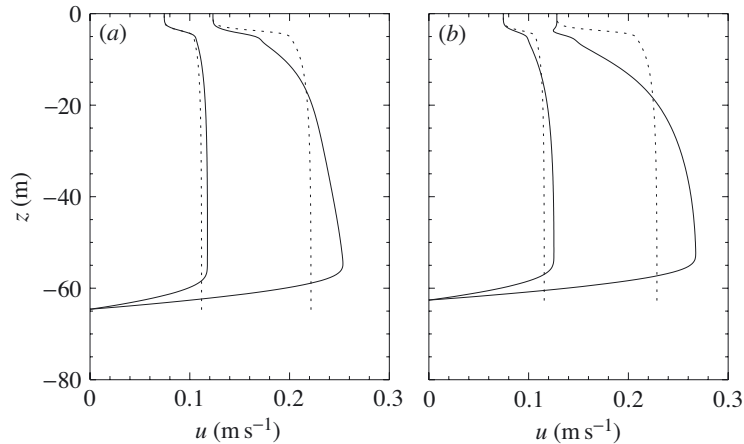
Figure 24. Comparison of theoretical (dotted) and model (solid) predicted vertical profiles of horizontal velocity at two different times (*a*) $x = -300$ m; (*b*) $x = -200$ m. The left pair of curves in each panel are at $t = \tau/32$. The right pair are at $t = \tau/16$.

the PP viscosity/diffusivity parametrization. A large lee wave was formed late in ebb flow, starting at approximately $t = 5\tau/16 = 0.3125\tau$. When the vertical eddy diffusivity was reduced by a factor of ten, the growth of the lee wave was limited and a high-drag state was not reached. Other model runs in which the eddy diffusivity was reduced did not produce this effect.

FA99 attributed the formation of a wedge of stagnant, near-surface fluid, resulting in transition to a high-drag state, to small-scale mixing associated with an instability of the flow over the top of the sill. They furthermore attributed the formation of the shear flow to the subcritical response early in the tidal cycle. The model runs presented in the preceding section show no indication of such instabilities and, with one exception, a large lee wave was formed. Why the apparent contradiction?

The results of §§ 3 and 4 show that lee-wave generation is inevitable unless boundary-layer separation occurs shortly after the ebb tide begins. Case I is one example of a model run for which a large lee wave was not formed. Small lee waves, confined to the pycnocline, were generated. This suggests that under the right conditions a large lee wave need not form.

Why were the observed shear flow instabilities during the early stages of ebb tide not modelled in these simulations? During the early stages of ebb tide a mode-1 wave is formed over the sill crest. Figure 24 shows vertical profiles of the horizontal velocity at $x = -300$ and $x = -200$ (parts (*a*) and (*b*) of figure 24, respectively) at $t = \tau/32 = 0.03125\tau$ and $\tau/16 = 0.0625\tau$ for case D. The velocity profiles are compared with the theoretically predicted profiles using the hydrostatic mode-1 linear eigenmode. The amplitude of the wave used in the theoretical profiles is chosen to match the model velocity at the top boundary. The fit is quite good at $x = -300$ m, particularly at the earlier time $t = \tau/32$. Closer to the sill crest at $x = -200$ m the flow increases with depth, relative to the linear mode-1 velocity, until the bottom boundary layer is reached. This difference is due to the growing lee wave centred just downstream of the sill crest at $x = 0$. The lee wave acts to slow down the fluid in the upper half of the water column and accelerate it in the lower half. The effect becomes more pronounced with time and by $t = \tau/16$ is apparent at $x = -300$ m. The long

mode-1 wave over the top of the sill produces a strong shear layer *ca.* 5 m below the surface. As the mode-1 response over the sill grows, the Richardson number decreases, providing a possible mechanism for the creation of an unstable flow. For case D, at $t = \tau/16$, the minimum Richardson number (outside the bottom boundary layer) is *ca.* 70 at $x = -300$ m, decreasing to *ca.* 10 at $x = -100$ m and *ca.* 2 at $x = 0$. The latter minimum value occurs at a depth of *ca.* 30 m and is due to a combination of baroclinic shear production and straining of isopycnals in the lee wave. By $t = \tau/8$ the minimum Richardson number at $x = -300$ m has decreased to 2.5. At $x = -100$ it has decreased to 0.3. The only values below 0.25 occur in the overturning lee wave.

The conclusion then, is that, at least outside the bottom boundary layer, the flow over the sill is stable until the lee wave overturns. This contradicts the observations which show the presence of small-scale instabilities. One possible reason for the absence of small-scale instabilities in the model results is that the density field used in the model simulations, which is based on observations over 1.2 km away, is not accurate enough in the region over the sill. Another contributing factor could be a background shear flow such as an exchange flow over the sill, however fig. 7(ii) of FA99 suggests that this is weak, if at all present, at the beginning of ebb tide. Some model simulations have been done using a density field with a sharper pycnocline and much higher resolutions ($\mathrm{d}x = 50$ cm, $\mathrm{d}z = 20$ cm over the sill) for which shear instabilities in the subcritical response over the sill are generated, in addition to the lee wave response. Available computational resources have limited model run times and at this time no connection between these instabilities and the formation of a wedge of stagnant fluid has been made. It is hoped that this can be explored more fully in the future.

Appendix A.

As an example of potential flow over an obstacle with an analytic solution, consider an infinitely deep layer of fluid flowing over a half-disc of radius a. With lower boundary at

$$z = h(x) = \begin{cases} 0, & \text{if } |x| \geqslant a, \\ \sqrt{a^2 - x^2}, & \text{if } |x| < a, \end{cases} \tag{A 1}$$

and far field flow $U(t)$ in the x-direction, the velocity potential is

$$\phi = U(t)\left[1 + \frac{a^2}{x^2 + z^2}\right]x. \tag{A 2}$$

From Bernoulli's theorem we have

$$\phi_t + p + \tfrac{1}{2}\nabla\phi \cdot \nabla\phi = C(t), \tag{A 3}$$

where $C(t)$ is a function of time (we recall that the pressure has been scaled by the reference density).

Along $z = 0$, for $|x| > a$, the pressure field is

$$p = C(t) - U'(t)\left(x + \frac{a^2}{x}\right) - \tfrac{1}{2}U^2(t)\left(1 - \frac{a^2}{x^2}\right)^2. \tag{A 4}$$

Evaluating at the left stagnation point at $x = -a$ gives

$$C(t) = p_{\text{sp}}(t) - 2aU'(t), \tag{A 5}$$

where $p_{\text{sp}}(t) = p(-a, 0, t)$ is the pressure at the left stagnation point. The pressure at the right stagnation point at $(x, z) = (a, 0)$ is $p_{\text{sp}}(t) - 4aU'(t)$.

Over the surface of the half-disc the pressure field is

$$p = C(t) - 2aU'(t)\cos\theta - 2U^2(t)\sin^2\theta. \tag{A 6}$$

Integrating the x-component of $-\int p\hat{n}\,\mathrm{d}s$ over the surface of the half-disc shows that the net horizontal force acting on the disc is

$$F_x = \pi a^2 U'(t). \tag{A 7}$$

This is non-zero for an accelerating flow, illustrating the fact that, for stratified tidal flow over a sill, part of the form drag on the sill is not associated with internal wave generation. In a reference frame fixed with the fluid at infinity, in which the disc is oscillating, fluid must be accelerated as the disc accelerates. The work done by the disc to accelerate the fluid is reflected in the non-zero value of F_x. This is referred to as the added mass effect.

From (A 6), it can be shown that the pressure has a minimum at

$$\cos\theta = \frac{aU'}{2U^2}, \tag{A 8}$$

provided that $a|U'| < 2U^2$. If $a|U'| > 2U^2$, the pressure decreases/increases monotonically along the surface, depending on the sign of U'. For weak acceleration, with $0 < U' < 2U^2/a$, the pressure minimum is to the right of the crest. For weak deceleration it is to the left.

For sinusoidal flow $U(t) = U_0 \sin(\omega t)$ and

$$\frac{aU'}{2U^2} = \frac{a\omega}{2U_0}\frac{\cot(\omega t)}{\sin(\omega t)}. \tag{A 9}$$

For small t there is no pressure minimum. As t increases to $\pi/(2\omega)$, the time of maximum flow, $aU'/2U^2$ decreases monotonically to zero. At some point $aU'/2U^2 = 1$. At this time the pressure has a minimum at $x = a$, the right stagnation point. As t increases the location of the pressure minimum moves to the left until at the time of maximum flow, when $U' = 0$, the pressure minimum is at the crest at $x = 0$. As the flow decelerates, the pressure minimum continues to move to the left, until it reaches the left stagnation point when $aU'/2U^2 = -1$.

References

Afanasyev, Ya. D. & Peltier, W. R. 2001*a* On breaking internal waves over the sill in Knight Inlet. *Proc. R. Soc. Lond.* A **457**, 2799–2825.

Afanasyev, Ya. D. & Peltier, W. R. 2001*b* Reply to comment on the paper 'On breaking internal waves over the sill in Knight Inlet'. *Proc. R. Soc. Lond.* A **457**, 2831–2834.

Armi, L. & Farmer, D. 2002 Stratified flow over topography: bifurcation fronts and transition to the uncontrolled state. *Proc. R. Soc. Lond.* A **458**, 513–538.

Baines, P. G. 1982 On internal tide generation models. *Deep-Sea Res.* **29**, 307–338.

Baines, P. G. 1995 *Topographic effects in stratified flows.* Cambridge University Press.

Blasius, H. 1908 Grenzschichten in Flüssigkeiten mit kleiner Reibung. *Z. Math. Phys.* **56**, 1–37.

Caulfield, C. & Peltier, W. 1994 Three dimensionalization of the stratified mixing layer. *Phys. Fluids* **6**, 3803–3805.

Cummins, P. F. 2000 Stratified flow over topography: time-dependent comparisons between model solutions and observations. *Dynam. Atmos. Oceans* **33**, 43–72.

Farmer, D. & Armi, L. 1999 Stratified flow over topography: the role of small-scale entrainment and mixing in flow establishment. *Proc. R. Soc. Lond.* A **455**, 2827–2830.

Farmer, D. & Armi, L. 2001 Stratified flow over topography: models versus observations. *Proc. R. Soc. Lond.* A **457**, 3221–3258.

Farmer, D. M. & Freeland, H. J. 1983 The physical oceanography of fjords. *Prog. Oceanogr.* **12**, 147–220.

Farmer, D. M. & Smith, J. D. 1980 Tidal interaction of stratified flow with a sill in Knight Inlet. *Deep-Sea Res.* A **27**, 239–254.

Gheusi, F., Stein, J. & Eiff, O. S. 2000 A numerical study of three-dimensional orographic gravity-wave breaking observed in a hydraulic tank. *J. Fluid Mech.* **410**, 67–99.

Hoinka, K. P. 1985 A comparison of numerical simulations of hydrostatic flow over mountains with observations. *Mon. Weather Rev.* **113**, 719–735.

Huppert, H. E. & Britter, R. E. 1982 Separation of hydraulic flow over topography. *J. Hydraul. Div. ASCE* **108**, 1532–1539.

Klaasen, G. & Peltier, W. 1985 The influence of stratification on secondary instability in free shear layers. *J. Fluid Mech.* **155**, 1–35.

Klemp, J. B. & Lilly, D. K. 1975 Dynamics of wave-induced downslope winds. *J. Atmos. Sci.* **32**, 320–339.

Klymak, J. M. & Gregg, M. C. 2001 Three-dimensional nature of flow near a sill. *J. Geophys. Res.* **106**, 22 295–22 311.

Klymak, J. M. & Gregg, M. C. 2003 The role of upstream waves and a downstream density-pool in the growth of lee-waves: stratified flow over the Knight Inlet sill. *J. Phys. Oceanogr.* **33**, 1446–1461.

Lamb, K. G. 1994 Numerical experiments of internal wave generation by strong tidal flow across a finite amplitude bank edge. *J. Geophys. Res.* **99**, 843–864.

Mellor, G. L. & Yamada, T. 1985 Modelling vertical and horizontal diffusivities with a sigma coordinate system. *Mon. Weather Rev.* **113**, 1380–1383.

Nash, J. D. & Moum, J. N. 2001 Internal hydraulic flows on the continental shelf: high drag states over a small bank. *J. Geophys. Res.* **106**, 4593–4612.

Pacanowski, R. C. & Philander, S. G. H. 1981 Parameterization of vertical mixing in numberical models of tropical oceans. *J. Phys. Oceanogr.* **11**, 1443–1451.

Peltier, W. R. & Clark, T. L. 1979 The evolution and stability of finite-amplitude mountain waves. II. Surface drag and severe downslope windstorms. *J. Atmos. Sci.* **36**, 1498–1529.

Queney, P. 1948 The problem of airflow over mountains: a summary of theoretical studies. *Bull. Am. Meteorol. Soc.* **29**, 16–26.

Schlichting, H. 1979 *Boundary-layer theory.* McGraw-Hill.

Scinocca, J. F. & Peltier, W. R. 1989 Pulsating downslope windstorms. *J. Atmos. Sci.* **46**, 2885–2914.

Winters, K. & D'Asaro, E. 1994 Three dimensional wave instability near a critical level. *J. Fluid Mech.* **272**, 255–284.